

Short-Range Recordings of Shallow Underwater Explosions with Short-Period and Broadband Seismometers in the Bay of Hyères, France

Mickaël Bonnin¹, E. Diego Mercerat², Éric Beucler¹, Nathalie Favretto-Cristini³, Anne Deschamps⁴, David Ambrois⁴, and Thierry Garlan⁵

ABSTRACT

This study presents the analysis of the seismic records of eight underwater explosions triggered by the French Navy Mine Warfare Office in December 2018 in the Bay of Hyères, southeast France. The explosions (charges of 80–680 kg TNT-equivalent) were recorded by 17 temporary stations composed of medium-to-broadband velocimeters and accelerometers and of microelectromechanical systems accelerometers with sampling rates of 250 or 500 samples per second, installed at less than 10 km from the sources. The relatively high sampling rates used in this study allow us to observe, at the same time, seismic, hydroacoustic, and acoustic signals at the shore. This experiment offers a unique opportunity to investigate the impact at the shore, and in the water, of relatively large-charge weight detonations as well as of the amplification effects of the sedimentary cover. We notably see that the hydroacoustic signal is, at the rocky sites, the most energetic wavepacket recorded, and that its observation seems to be conditioned by the bathymetry and the seabed sedimentary cover. We also show that the hydroacoustic phase can be advantageously used to precisely estimate the location and origin time of the explosions. Finally, analyses of the spectrum and site response along the shore and at a bell tower on the Porquerolles Island provide interesting insights on the mitigation of the possible nuisance caused at the shore by the disposal of unexploded historical ordnance.

KEY POINTS

- The present study investigates the explosion-induced seismic signals received at the shore during unexploded historical ordnance (UXO) disposal.
- Energy received at the shore depends on the configuration of the explosion on the bathymetry and geology.
- Mitigation of the nuisances caused by UXO disposal requires more investigation, as geology plays a major role.

[Supplemental Material](#)

INTRODUCTION

Unexploded historical ordnance (UXO) from World War II are discovered almost every week on the northwestern and southeastern coasts of metropolitan France. Quickly after their discovery, the French Navy Mine Warfare Office (FNMWO) must destroy the munitions to ensure the safety of divers and ships. The favored destruction method is countermining, that is, to use a high-order detonation conducted by exploding an additional donor charge placed adjacent to the UXO. Depending on whether the UXO is safe to move, such countermining occurs at specific safe locations or at the location of the

discovery. When the UXO is safe to move, the FNMWO usually gathers several UXO to reduce the number of explosions. As a result, global charges of several hundreds of kilograms equivalent trinitrotoluene (TNT) can be detonated at once.

The risks for people in charge of the UXO countermining are well known by the Mine Warfare experts. The UXO clearance is also known to disturb or to harm the marine wildlife (e.g., von Benda-Beckmann *et al.*, 2015). In contrast, it is difficult to reliably evaluate the possible consequences of

1. Laboratoire de Planétologie et Géosciences, Nantes Université, Univ Angers, Le Mans Univ, CNRS, Nantes, France, <https://orcid.org/0000-0003-2909-1375> (MB); <https://orcid.org/0000-0003-2605-4990> (ÉB); 2. Équipe REPSODY, CEREMA Méditerranée, Sophia-Antipolis, France, <https://orcid.org/0000-0003-3154-584X> (EDM); 3. Aix-Marseille Univ., CNRS, Centrale Marseille, LMA, Marseille, France, <https://orcid.org/0000-0002-9447-3647> (NF-C); 4. Université Côte d'Azur, CNRS, Observatoire de la Côte d'Azur, IRD, Valbonne, France, <https://orcid.org/0000-0002-6209-9814> (AD); <https://orcid.org/0000-0003-1155-5645> (DA); 5. Marine Geology Department, Shom/DOPS/STM/SEDIM, Brest Cedex 2, France, <https://orcid.org/0000-0002-5354-5587> (TG)

*Corresponding author: mickael.bonnin@univ-nantes.fr

Cite this article as Bonnin, M., E. D. Mercerat, É. Beucler, N. Favretto-Cristini, A. Deschamps, D. Ambrois, and T. Garlan (2022). Short-Range Recordings of Shallow Underwater Explosions with Short-Period and Broadband Seismometers in the Bay of Hyères, France, *Bull. Seismol. Soc. Am.* **XX**, 1–19, doi: [10.1785/0120220141](https://doi.org/10.1785/0120220141)

© Seismological Society of America

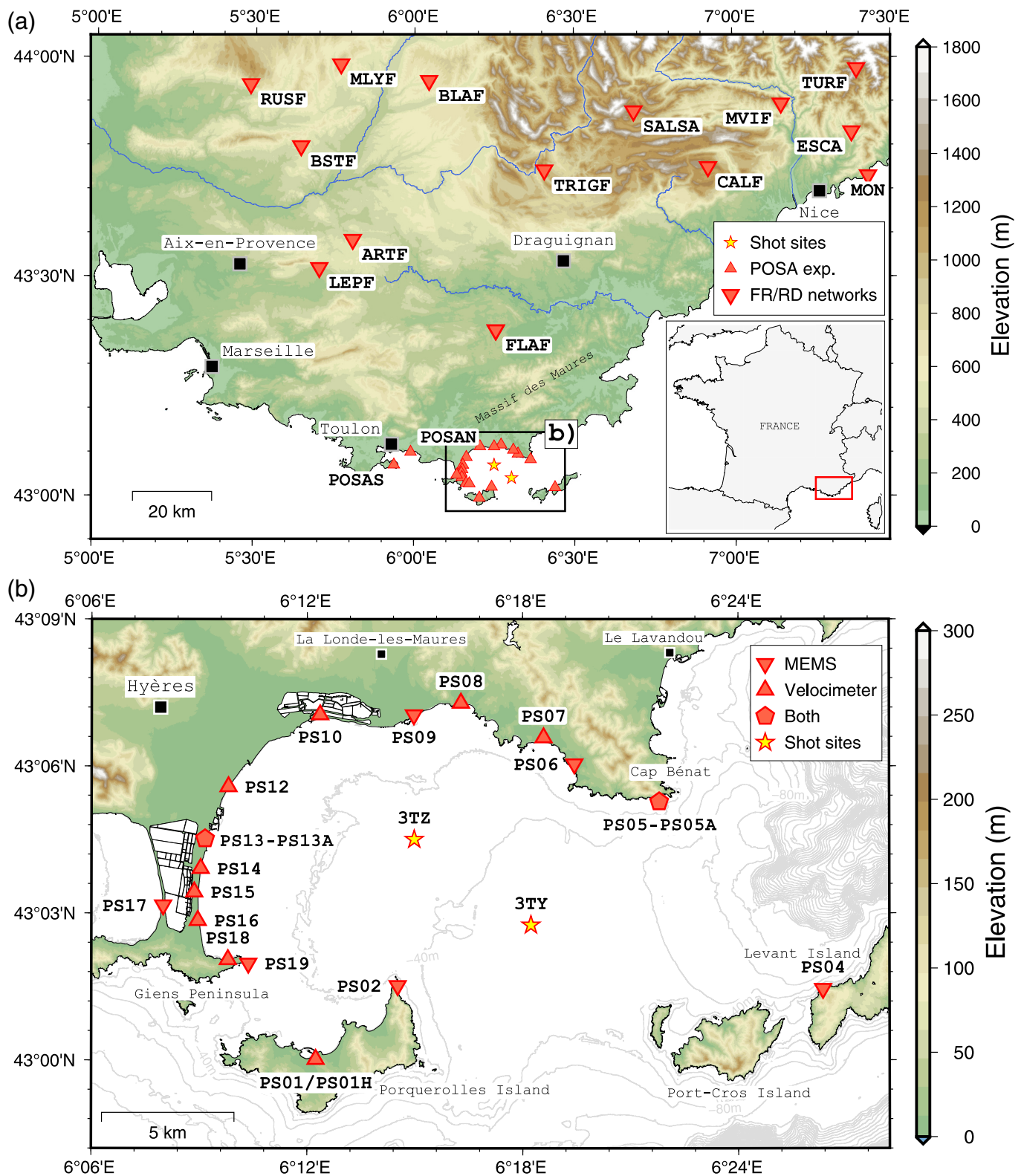


Figure 1. (a) Map of the French permanent broadband seismic stations in the southeast France and (b) of the temporary seismic stations deployed in the Bay of Hyères. The locations labeled 3TY and 3TZ are the locations where the explosive charges were detonated. The thin gray curves in (b) indicate the bathymetry (contours are plotted every 20 m and are labeled every

40 m). The inset shows the localization of metropolitan France in western Europe. The red rectangle indicates the position of the map on the panel (a) in the SE France. The color version of this figure is available only in the electronic edition.

underwater explosions on the marine environment and on the buildings located on the nearest coast. Indeed, they depend mostly on the environment geology and on the characteristics (weight and location) of the explosive charges and, hence, on the detonation-induced wave propagation. Large underwater explosions may trigger small-scale landslides that could, in turn, generate large waves on the shore or damage infrastructures (pipelines, optic fibers). Therefore, there is a need for developing a decision support tool for the risk assessment regarding inland infrastructures before clearance of UXO of large weights.

One of the main goals of the characteristics of the propagation of anthropogenic seismic waves (POSA) project (2016–2018), partly funded by the French Navy, was to pave the way for reliably assessing the risk of building damage on the adjacent shore, induced by the detonation of large-charge UXO (of between 80 and 680 kg TNT-equivalent weights) in a variable shallow water environment with a water depth less than 50–100 m. Although the wave propagation generated by the detonation of small charges (usually, smaller than a few-kilograms TNT-equivalent weight) is quite well studied in the open literature (e.g., Chapman, 1985; Nolet and Dorman, 1996; Soloway and Dahl, 2014), to the best of our knowledge, very few studies are concerned with charges of a few hundred kilograms TNT-equivalent weight and located in coastal waters with a depth close to 50–100 m (Hunter and Geers, 2004; von Benda-Beckmann *et al.*, 2015; Gitterman and Sadwin, 2017; Salomons *et al.*, 2021). In that respect, the POSA project can be considered as a pioneer work.

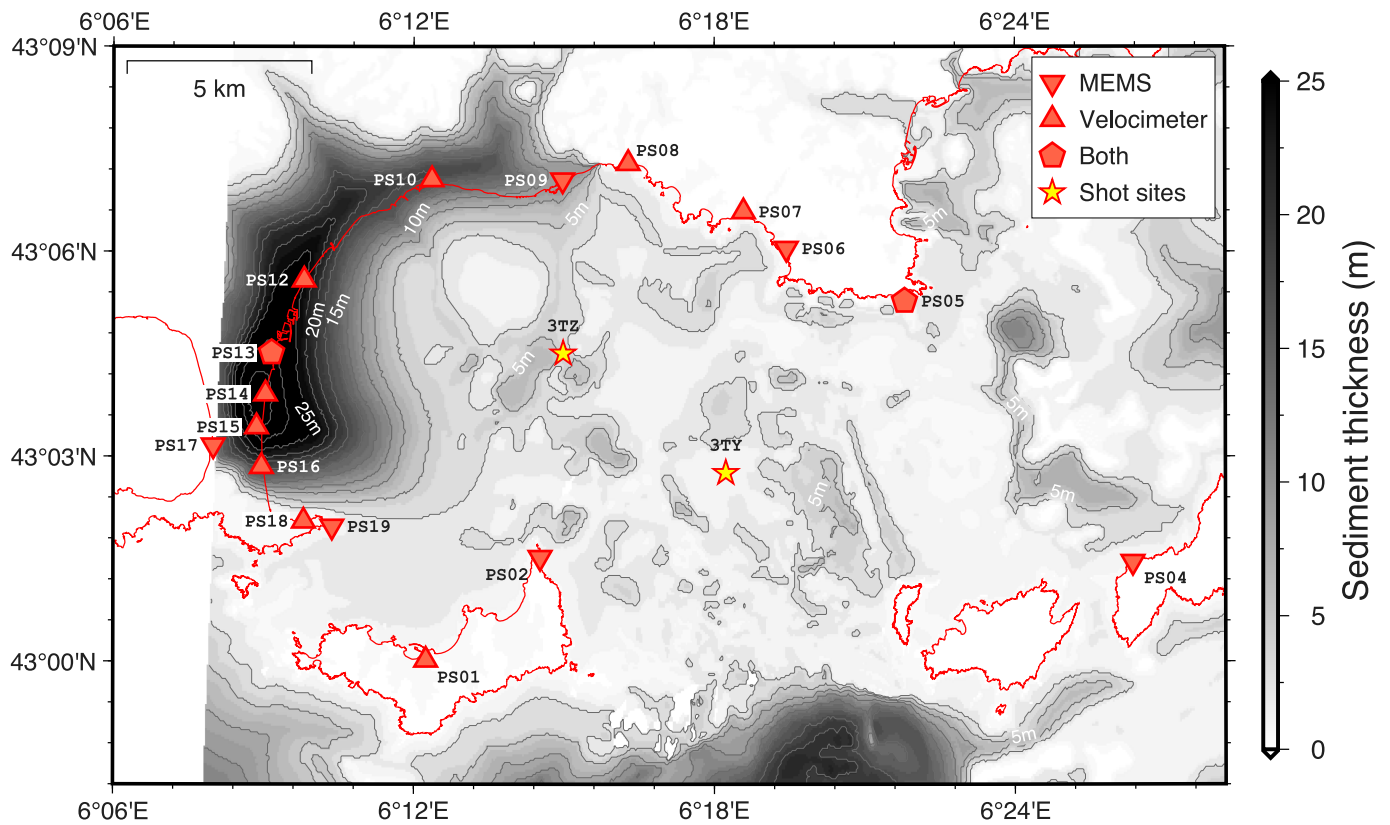
To understand how the seabed (and possibly, the viscoelastic sedimentary layer with a varying thickness) and the water column (with a varying depth) influences the propagation of the seismoacoustic waves that are generated by the UXO detonation and that reach the coast, we have relied on a multidisciplinary cross study, including data obtained within the framework of controlled countermining campaigns and numerical simulations of the seismoacoustic propagation using a spectral element method. The countermining campaigns were conducted in December 2018 in the Mediterranean Sea, in the Bay of Hyères (southeastern part of France, Fig. 1). The data have been recorded by acoustic recording systems (namely, two hydrophones and one shock gauge) and by a relatively dense array of seismic stations (velocimeters and accelerometers) located on the shore at the maximum of 15 km from the underwater explosion locations. Most of the results obtained from the analysis of the real acoustic and seismic data and from the numerical simulations are reported in a two-companion paper (Favretto-Cristini, Garlan, *et al.*, 2022; Favretto-Cristini, Wang, *et al.*, 2022). In particular, it has been shown that, compared to a charge detonation in water, a similar detonation on the seabed generates seismic signals of much lower frequencies (<30 Hz) and higher amplitudes that propagate in the seabed. It has also been shown that the ground acceleration is linearly related to the charge weight. Favretto-Cristini, Garlan, *et al.* (2022) have thus derived two empirical laws

for the induced local seismic magnitude as a function of the charge weight for the case of a charge detonation in the water column and on the seabed, respectively. Overall, the two laws follow the same trend but with a shift of 0.5 in magnitude, because much less energy is transmitted downward into the ground when the explosion takes place at a shallow depth in water. Some complementary and very interesting results have also been obtained from high sampling rate data (500 samples per second) recorded by microelectromechanical systems (MEMS) accelerometers that are both cheaper and easier to deploy than conventional high-sensitivity accelerometers. The present study mainly focuses on these original records, in particular, the contribution of phases that are not recorded by conventional sensors at the usual sampling rates (less than 250 samples per second). In addition, the impact of underwater explosion-induced waves on the nearby engineering structures is also illustrated.

The article is organized as follows. The POSA experiment in 2018 section briefly describes the POSA experiment conducted in the Bay of Hyères in December 2018, namely the geological environment, the characteristics (weight and location) of the detonated charges, and both the permanent and the temporarily deployed seismic networks. The explosion-induced seismic signals section then presents the explosion-induced seismic signals recorded by the temporary network, with a focus on the signals recorded by the MEMS accelerometers. It is shown that this kind of accelerometers allows for observing, at some sites, hydroacoustic waves (*H* phases) that can be used to better estimate the location and origin time of the explosions (see the Contribution of the *H*-phase to the Improvement in Signal Analysis section). In addition, the seabed explosions generate a complex source pattern observed at most of the temporary stations. The contribution of the *H*-phase to the Improvement in Signal Analysis section also discusses the impact of the charge characteristics on the recorded signals. Finally, the Ground response to the explosion-induced seismic motion section investigates the influence of the environment geology on the explosion-induced seismic signals recorded on the shore and illustrates the impact of the underwater explosions on a nearby engineering structure located on the Porquerolles Island.

POSA EXPERIMENT IN 2018 Geological settings of the Bay of Hyères

The Bay of Hyères is located at the southwestern edge of the Massif des Maures—a late Proterozoic–Paleozoic crystalline massif in southeast France (Fig. 1a). The Bay of Hyères extends from the Giens Peninsula (West) to the Cap Bénat and the Levant Island (East) (Fig. 1b). It is approximately 15 km long in the east–west direction and 10 km wide in the north–south direction. Mean water depth is about 40 m with slopes gently dipping eastward, but water depth rapidly increases to several hundred meters due to the presence of submarine canyons at east of the Cap Bénat and south of the Porquerolles and Port-Cros Islands (Fig. 1b). On land, outcropping rocks consist of Paleozoic metasediments



and metamorphic rocks (mostly slate, schist, and gneiss [e.g., Chantraine *et al.*, 2003]). On the shore (especially on the tombolo of the Giens Peninsula and near the salt marshes at the northwestern part of the bay) and on the seabed of the bay, these rocks are covered by unconsolidated quaternary sediments (mostly sands). The sedimentary cover is generally less than 5 m thick within the bay but locally reaches 30 m in the southernmost part of the tombolo of the Giens Peninsula (Fig. 2). Our knowledge of the bathymetry and of the nature of the sediments is quite robust, as they were provided by specific acoustic and geological high-resolution surveys conducted before the experiment (Favretto-Cristini, Garlan, *et al.*, 2022). The sediment properties are, at the first order, constant within the whole experiment area (see table 1 of Favretto-Cristini, Garlan, *et al.*, 2022), except close to the western part of the bay.

Characteristics of the detonated charges

Eight explosive charges (hereafter, labeled S1–S8) were detonated at two sites in the Bay of Hyères (see Fig. 1b), on December 2018. Three (S1–S3) were detonated on 11 December and five (S4–S8) on 12 December. The first explosion site (3TZ) is located on the sea bottom at approximately 29 m of water depth, above approximately 4–5 m of unconsolidated sediments, whereas the second site (3TY) is located at approximately 46 m of water depth, above approximately 1–2 m of unconsolidated sediments (Fig. 2).

To have a good control on the charge weight, the FNMWO chose to replace the real UXO by specific cylindrical explosive charges. Half of the charges (S1, S2, S3, and S8) were charges of

Figure 2. Map of the unconsolidated sediment thickness in the Bay of Hyères (contours every 2.5 m). The red curves correspond to the shore line. Symbols for stations and detonation sites are the same as in Figure 1. The color version of this figure is available only in the electronic edition.

80 kg TNT-equivalent filled with tritonal 80/20 (80% of TRInitroToluene and 20% of ALuminium [TRITONAL] powder). The source S7 was a charge of 200 kg TNT-equivalent filled with HBX-3. The others (S4, S5, and S6) had a weight of 680, 600, and 400 kg TNT-equivalent, respectively, and consisted of bundles of the smaller cylindrical charges (of 80 and 200 kg TNT-equivalent) stacked together in a container.

TABLE 1
Characteristics of the Detonated Charges

Code	Site	Weight (kg TNT-Equivalent)	Configuration
S1	3TZ	80	Seabed
S2	3TZ	80	Seabed
S3	3TY	80	Seabed
S4	3TY	680	Seabed
S5	3TY	600	Seabed
S6	3TY	400	Seabed
S7	3TY	200	Seabed
S8	3TY	80	Water column

The explosion sites 3TZ and 3TY were localized by the French Navy Mine Warfare Office (FNMWO) at 43.075107° N/6.249712° E and 43.045968° N/6.303822° E, respectively. TNT, trinitrotoluene.

TABLE 2

Characteristics of the Seismic Instruments

Code	Lat. (°)	Long. (°)	Elev. (m)	Instr. Name	Instr. Type	Samp. Rate (Samples Per Second)
PS01	43.0003	6.20400	2	CMG40-T	VEL	250
PS01H	43.0003	6.20400	14	CMG40-T	VEL	250
PS02	43.0253	6.24200	23	DSU3-428	ACC	500
PS04	43.0243	6.43917	9	DSU3-428	ACC	500
PS05	43.0880	6.36333	48	CMG40-T	VEL	250
PS05	43.0880	6.36333	48	ES-T	ACC	250
PS05A	43.0880	6.36333	48	DSU3-428	ACC	500
PS06	43.1007	6.32400	2	DSU3-428	ACC	500
PS07	43.1097	6.30967	4	CMG-6T	VEL	250
PS08	43.1215	6.27133	1	CMG-6T	VEL	250
PS09	43.1175	6.24950	2	DSU3-428	ACC	500
PS10	43.1175	6.20600	0	CMG-6T	VEL	250
PS12	43.0930	6.16350	2	CMG40-T	VEL	250
PS13	43.0753	6.15267	2	CMG40-T	VEL	250
PS13A	43.0753	6.15267	2	DSU3-428	ACC	500
PS14	43.0652	6.15067	0	CMG40-T	VEL	250
PS15	43.0572	6.14767	2	CMG-6T	VEL	250
PS16	43.0475	6.14933	2	CMG40-T	VEL	250
PS17	43.0527	6.13333	1	DSU3-428	ACC	500
PS18	43.0342	6.16333	12	CMG-6T	VEL	250
PS19	43.0328	6.17283	7	DSU3-428	ACC	500

Elev., elevation; instr., instrument; lat., latitude; lon., longitude; and samp., sampling.

Two countermining configurations were chosen corresponding to the protocols used by the French Navy to destroy UXO: (1) charges lying on the seabed (S1–S7) and (2) a charge installed in a barrel floating at approximately 11 m depth in the water column (S8). The former are suspected to generate large amplitude seismic waves on land due to the physical coupling of the source with the seabed. The latter is not adapted to the largest charges frequently encountered, as fragments of shells can be ejected in the air when the barrel is too close to the surface. As this protocol reduces the coupling with the ground, it is thus expected to mitigate the low-frequency seismic energy that could be felt on land (Favretto-Cristini, Garlan, *et al.*, 2022; Favretto-Cristini, Wang, *et al.*, 2022). It however releases much more energy in the water column and is thus likely to have a more negative impact on the marine wildlife. The characteristics of the charges are summarized in Table 1.

Permanent stations available at regional distances

As the Provence region and the French Riviera are among the most seismically active zones in metropolitan France (e.g., Cara *et al.*, 2015; Larroque *et al.*, 2022), a relatively dense array of broadband seismometers is available in the vicinity of the POSA experiment (Fig. 1a). Permanent stations are operated by the *Observatoire de la Côte-d'Azur* (OCA) and the *Commissariat à l'Énergie Atomique et aux énergies alternatives* (CEA, station FLAF), and are part of the Résif-EPOS network (RESIF, 1995).

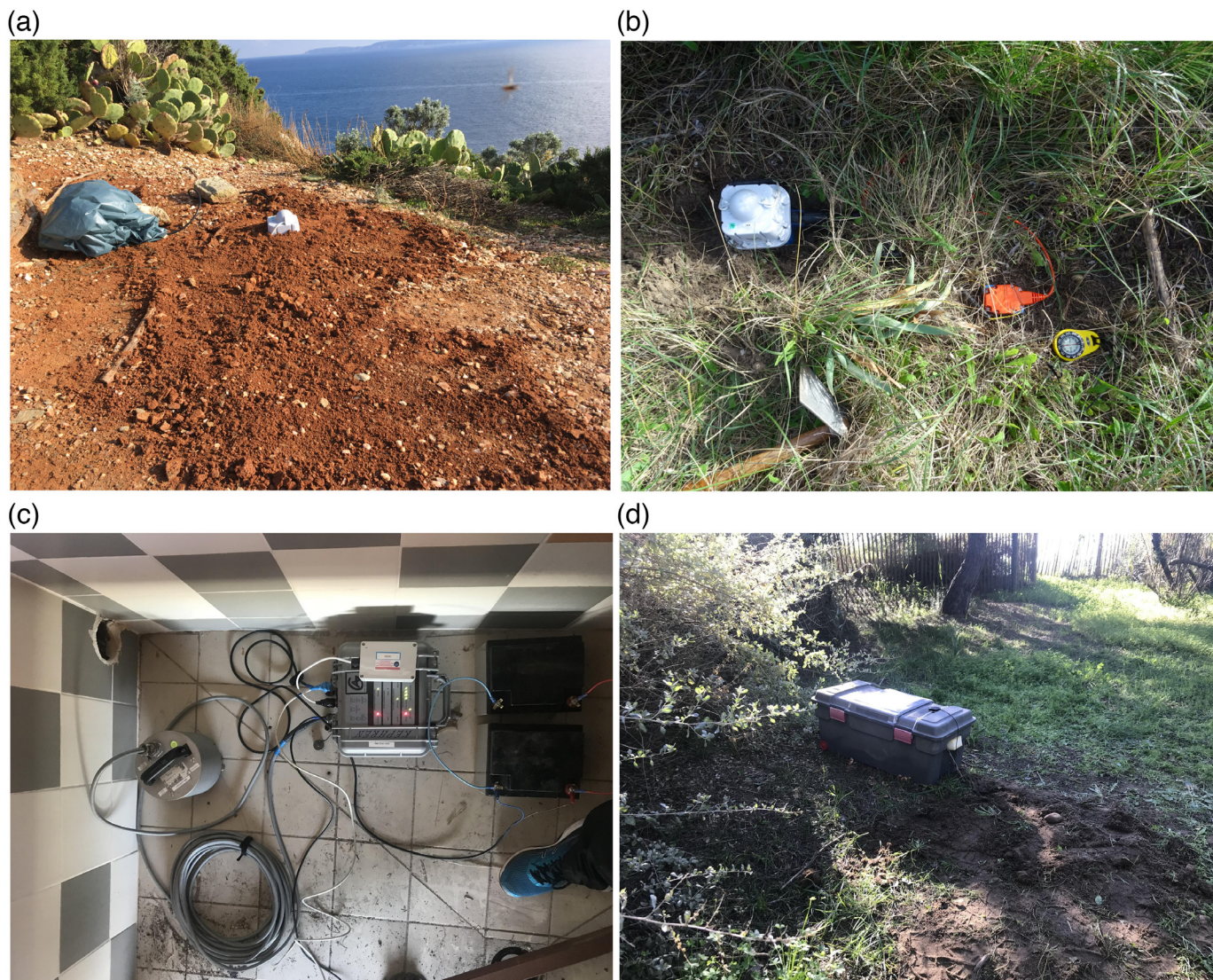
However, the closest permanent station (FLAF, Fig. 1a) is located at about 40 km from the Bay of Hyères, and the

azimuthal gap due to the geometry of the network used routinely for event location by the French institutions is approximately of 150°. Hypocentral solutions provided by these stations thus led to large uncertainties (as shown later in the [Inversion of onset times to better infer source locations and explosion times](#) section), especially in depth and in latitude (given the fact that none of the permanent stations is located south of the explosion sites). This problem is not specific to the Bay of Hyères but to most of the underwater explosions along the French coasts (in particular, in Brittany and in Normandy, northwest France).

Temporary network deployed around the Bay of Hyères

Given the limitation of the permanent seismic network, the precise observation of the explosions and of their impact on the coast required the deployment of a relatively dense temporary seismic network, installed some days before the explosion dates by several teams of the Géoazur laboratory, of the *Service hydrographique et océanographique de la Marine* (SHOM) and of the *Centre d'étude et d'expertise sur les risques, l'environnement, la mobilité et l'aménagement* (Cerema) Sophia-Antipolis.

This temporary seismic network was composed of 20 three-component medium-to-broadband velocimeters and accelerometers (Table 2) that were deployed at 17 sites along the coast at distances ranging from 6 to 13 km from the explosion locations (Fig. 1b). The seismic stations recorded continuously during their operation from early 11 December to late 12



December 2018, covering the whole FNMWO campaign period. Data from two other temporary stations (POSAS and POSAN, Fig. 1a) installed 30 km west, near the Toulon Roads, are also used to invert the source parameters.

One originality of the POSA experiment is the use of eight MEMS accelerometers (Sercel DSU3-428 in Table 2, see also Fig. 3 and the supplemental material available to this article) in complement to classical medium-to-broadband velocimeters and accelerometers. Besides their low cost, these instruments have the great advantage of being easily installed in remote locations (such as islands) without external power sources. To estimate the performance of these instruments, two of them were collocated with classical seismological stations at Cap Bénat (rocky site PS05-PS05A, Fig. 1b) and at Pesquiers (sandy site PS13, Fig. 1b). The comparison of the continuous seismic signal and the waveforms induced by the explosions recorded at the site PS05-PS05A is presented in the supplemental material. The site PS13 was very noisy for both MEMS accelerometers (PS13A) and velocimetric (PS13) recordings, and that the vertical component of the velocimeter

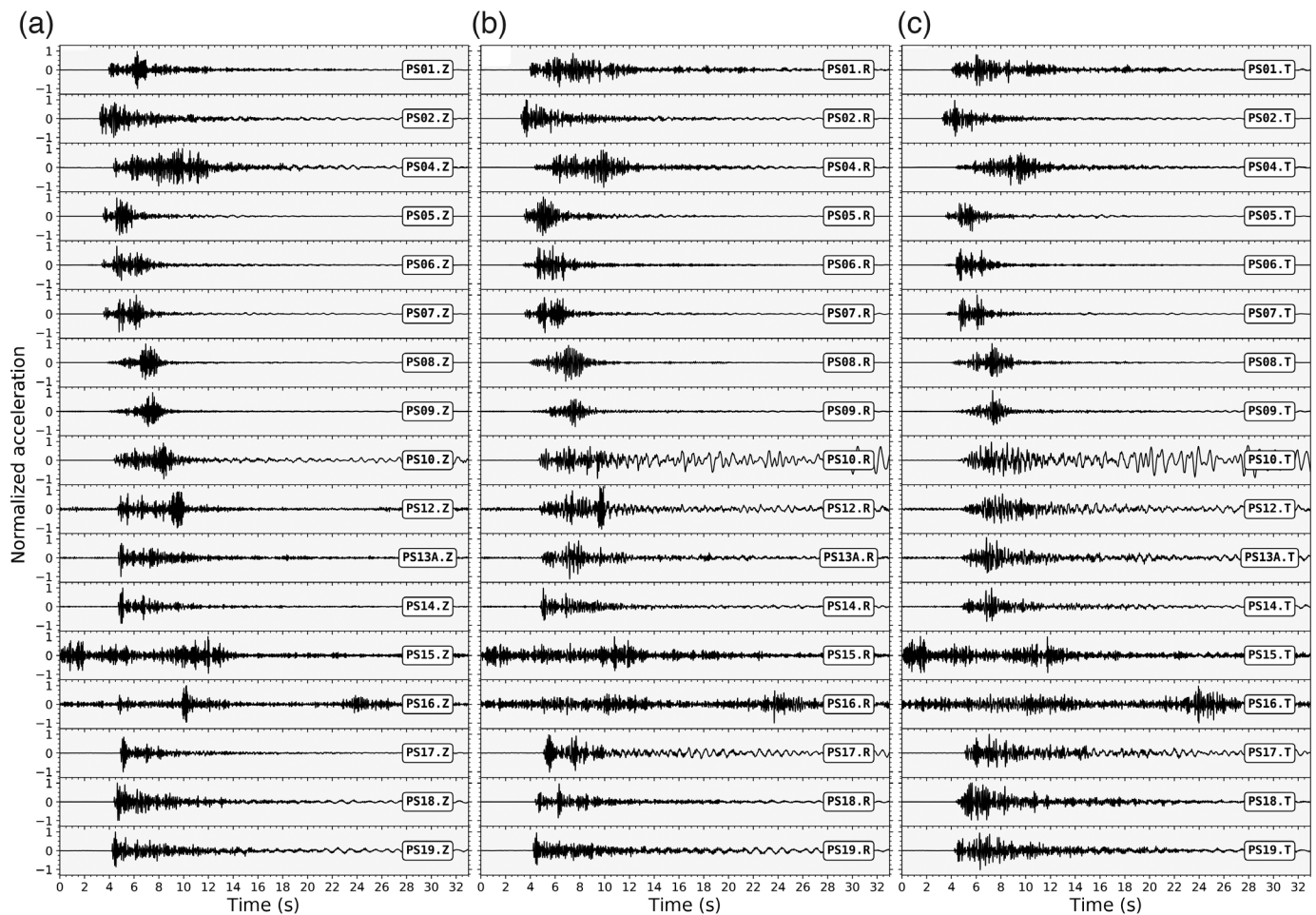
Figure 3. (a,b) Pictures of the installation of the microelectromechanical systems (MEMS) accelerometers at the (a) site PS05A (Cap Bénat) and the (b) site PS17 (Almanarre beach). (c,d) Pictures of velocimeter installations in (c) a building and in (d) open field. The color version of this figure is available only in the electronic edition.

unfortunately was out of order. Therefore, only the MEMS (PS13A) record is used in the study.

For the sake of illustration of the impact of underwater explosions on nearby civil engineering structures, two velocimeters that compose the station PS01 were located at the top (PS01H, placed at 12 m above the ground level) and the bottom (PS01) of the bell tower of the Sainte-Anne church located on the Porquerolles Island (Figs. 1b, 3). The church was chosen because of its ease of accessibility and because of the absence of any other high-rise building on the Porquerolles Island.

EXPLOSION-INDUCED SEISMIC SIGNALS

For the sake of illustration, the seismic traces generated by the explosion S4 (charge of 680 kg TNT-equivalent weight) and



recorded at all the sites are presented in Figure 4. The main seismic signal lasts about 10 s after onset time at the closest rocky sites but can last several tens of seconds at the sites on (PS10) or behind (PS17) the salt marshes. The largest amplitudes are generally observed for *S* waves and surface waves with amplifications that can be significant on the horizontal components, particularly at the sandy sites (for instance, site PS10).

The frequency content of the signals is mainly between 0.5 and 50 Hz (Fig. 5), with two principal peaks around 1 and 10 Hz. But, as shown in the [Observation of the *H* and *I* phases](#) section, hydroacoustic phases above 100 Hz can dominate the spectrum at some particular sites. In the following, we highlight and discuss some of these striking features on the explosion-induced seismic signals.

Observation of the *H* and *I* phases

The seismic traces recorded on land are characterized by three main wave packets (onsets shown as vertical dashed lines in Fig. 6). The first wave packet obviously corresponds to the *P* wave. The second one corresponds to the *S* wave, followed by surface waves that can be well observed for the sedimentary sites. In addition, a high-amplitude, high-frequency wave packet (labeled *H* in Fig. 6) is observed at some stations (mostly

Figure 4. Seismograms induced by the explosion S4 (charge weight of 680 kg trinitrotoluene [TNT]-equivalent) and recorded by the seismic stations: (a) vertical component, (b) radial component, and (c) transverse component. The traces are 20 Hz low-pass filtered. Note the significant variability in the signal duration (site PS10 with respect to site PS06, for instance). See Figure 1 for the station map.

at the stations with a sampling rate of 500 samples per second). This phase appears on the three components of the seismograms, but more clearly on the vertical one (black traces in Fig. 6) when the sampling frequency allows for recording frequencies well above 100 Hz (Table 2).

Considering that the stations PS05-PS05A are located at approximately 6.5 km from the explosion site 3TY, we can estimate from Figure 6 the apparent velocity of the third phase to be between 1.5 and 1.6 km s⁻¹. This velocity range is very close to the sound velocity in sea water (1.507 km s⁻¹ estimated from the water temperature measured during the experiment, Favretto-Cristini, Garlan, *et al.*, 2022). This wave packet thus very likely corresponds to acoustic energy that propagates within the water column from the source to a location close to the shore, and that subsequently converts to seismic energy before being recorded by the seismic sensor. The location where this conversion occurs is likely associated with the cutoff

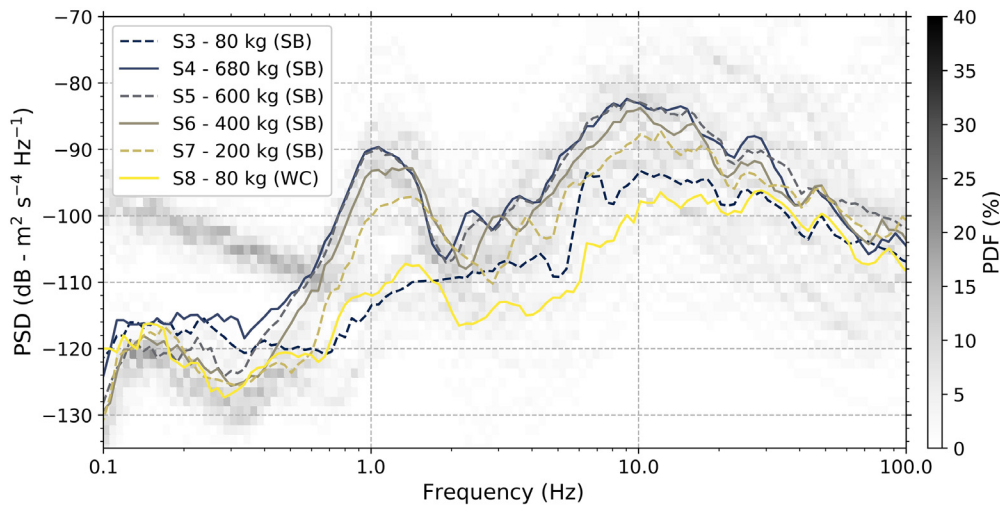


Figure 5. Median of the spectra computed from the vertical component of the seismograms recorded at all the seismic stations for charges detonated at the explosion site 3TY (solid and dashed curves). The grayed 2D histograms in the foreground shows the probability density function (PDF) of all the individual spectra (vertical components) recorded by all the stations for all the charges detonated at the explosion site 3TY. This illustrates the variability of the spectra recorded during the experiment. The bimodal distribution observed in the PDF at the lowest frequencies (below 1 Hz) is caused by the sensitivity difference between MEMS (the highest amplitudes) and velocimeters (the lowest amplitudes). The color version of this figure is available only in the electronic edition.

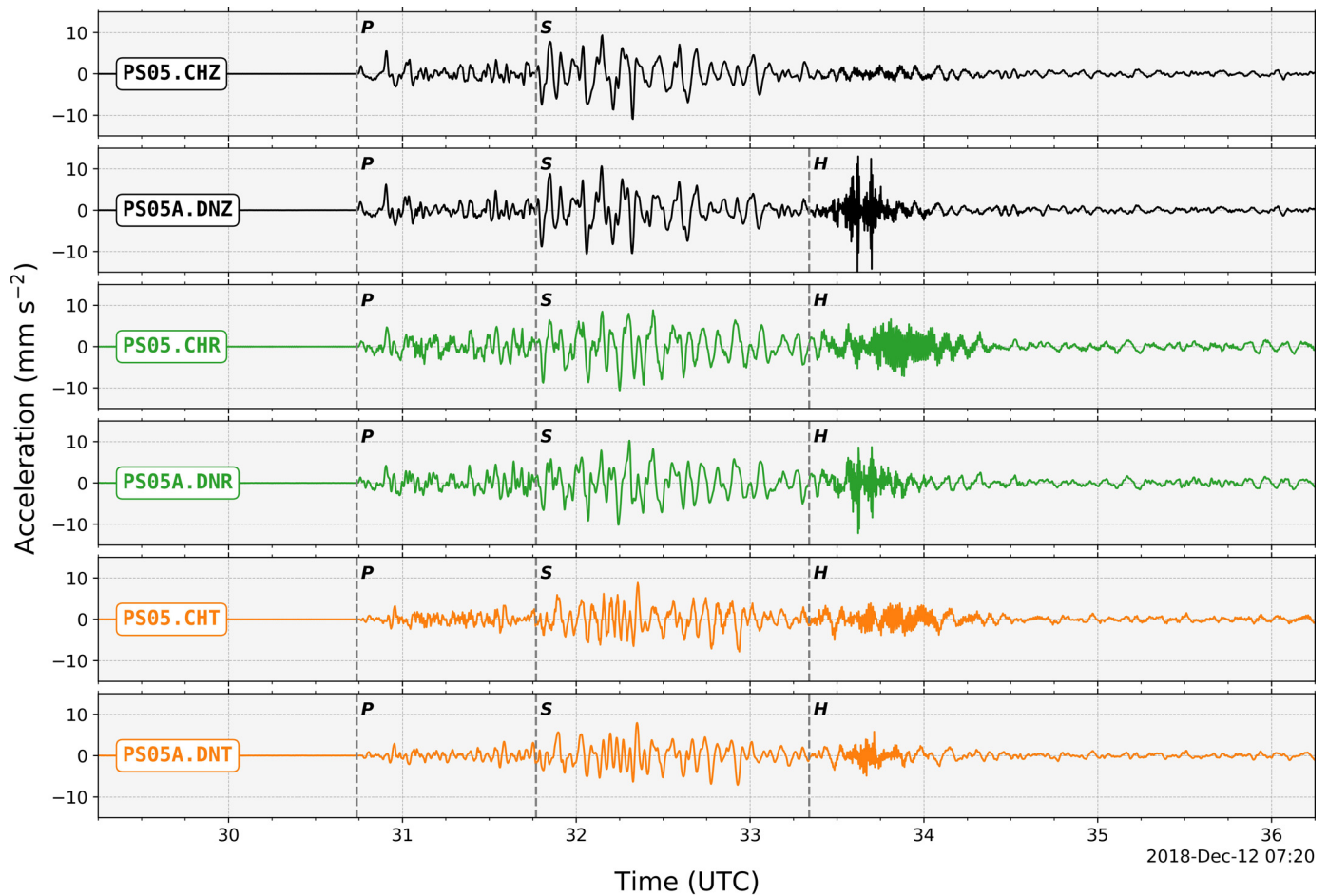
height of the acoustic modes, well known in underwater acoustics (Favretto-Cristini, Wang, *et al.*, 2022). The International Association of Seismology and Physics of the Earth's Interior (IASPEI) nomenclature for this type of phase is *H* (Bormann *et al.*, 2013), though this naming is often used to characterize energy recorded by hydrophones. The observation of a third wave in cases of underwater explosions is also named *T* phase in the literature (e.g., Kim and Gitterman, 2013; Heyburn *et al.*, 2018), but *T* phase is supposed to be generated by sources in the solid Earth (Bormann *et al.*, 2013), and to have propagated within the Sound Fixing and Ranging channel (e.g., Johnson *et al.*, 1963; Talandier and Okal, 1998; Buehler and Shearer, 2015). Therefore, as the third phase we observe in Figure 6 is definitely not a *T* phase, we hereafter use the term *H* phase to avoid any confusion.

Figure 7 shows the spectrograms obtained from the vertical component of the signals generated by the explosion S8 (charge of 80 kg TNT-equivalent weight located at the site 3TY in the water column) and recorded at the MEMS accelerometers (DSU3-428 in Table 2), with a Nyquist frequency of 250 Hz. The solid white arrows highlight the arrivals of the *H* phase. We can note that the spectrum of this phase is relatively broad, from generally 50 Hz to more than 200 Hz, with a dominant frequency that seems to be around 100 Hz. The lower frequency limit (50 Hz) can be even lower, for instance, at the station PS09. The *H*-phase wave packet in Figure 7 is composed of 2–3 arrivals separated by approximately 0.5 s (well visible at sites PS02 and PS04). These arrivals are likely due to the energy released in the water by the pulses of the gas globe generated by the

detonation (Cole, 1948). The *H* phase is observed at all the sites with high sampling rate (500 samples per second) records, with particularly large amplitudes at the stations PS02, PS05A, PS09, and PS04. These stations are located on the rocky parts of the coast (near the Cap Bénat in the northeast, on the islands, and in the southern part of the Giens Peninsula). The *H* phase thus faces relatively low attenuation, which is also a well-known characteristic of hydroacoustic phases. An interesting observation is that the highest amplitudes are observed at the stations PS09 and PS04 that are not the closest stations from the explosion. In particular, the *H* phase is clearly visible at the station PS04 (located at about

12 km from the explosion), whereas it is only slightly visible at the station PS06 that is located at approximately half this distance. Moreover, the signal appears unexpectedly very weak at the station PS19 that is located on a rocky site and almost at the same distance as the station PS04 from the explosion. At the largest distances from the explosion (see the stations PS13A and PS17 located on the tombolo of the Giens Peninsula), the *H* phase does no longer present a very high frequency content but exhibits a dispersion clearly observed in the spectral band 50–120 Hz. The high attenuation of the unconsolidated sediments, together with the gentle slopes at the coastal areas, can explain these observations. The complex behavior of the *H* phase is probably related to the difference in the bathymetric profiles between the western and northwestern stations where the water depth is less than 20 m far from the coast (mild slopes), and the eastern stations mostly located on cliffs and where the water depth is greater than 30 m close to the coast. This is confirmed by Talandier and Okal (1998) or more recently by Bottero *et al.* (2020) who have shown that the slope of the sea floor is a key parameter for the conversion of the hydroacoustic energy to seismic energy at the shore. Given the characteristics of the *H* phase (high amplitude, high frequency, and low attenuation), we suggest that this energy might be mainly responsible for the human perception of the underwater explosions near the shore.

From Figure 7 (top right, open white arrow), it can be seen that the station PS02 (the closest from the site 3TY) also recorded an energy packet with an apparent velocity of approximately 350 m s^{-1} , that is, close to the sound velocity in the air



(340 m s^{-1}). This energy packet can also be observed at this station for the explosions S4–S7 (Fig. S1). It is likely an acoustic phase that propagated in the air from the explosion location. Following the IASPEI convention (Bormann *et al.*, 2013), we refer this energy packet to the *I* phase.

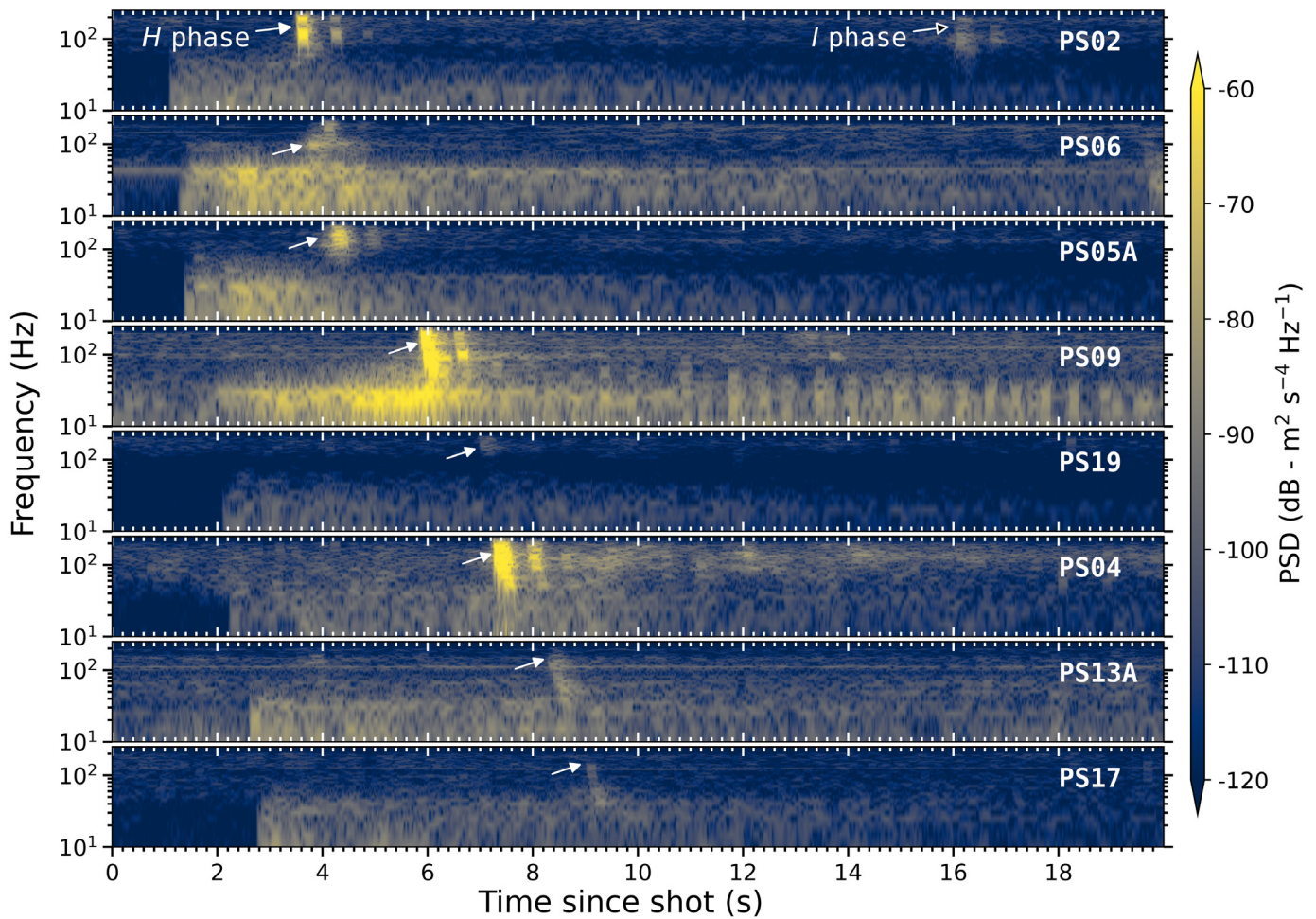
Observation of a second pulse after the *P*-wave onset

Figure 8 focuses on one second of the vertical component of the signals generated by the explosion of the different charges (S1–S8) and recorded by the stations PS05A, PS04, and PS19. The vertical component of the signals is low-pass filtered at 50 Hz, and the amplitudes are normalized.

When focusing on the first tenths of second, we observe that the first energy arrival is actually composed of two pulses separated by a time delay ranging from 0.08 to 0.15 s (arrows in Fig. 8). The first pulse arriving at 0.2 s corresponds to the *P* wave. The second pulse is surprisingly coherent in phase and amplitude ratio with the onset of the first energy pulse at the stations PS05A, PS04, and PS19 that are distant from the explosion site 3TZ by 9 km, 16 km, and 8 km, respectively, and from the explosion site 3TY by 7 km, 11 km, and 11 km, respectively (Fig. 1b). However, the waveforms after this second pulse rapidly lose their coherency between the stations.

Figure 6. Comparison of acceleration traces induced by the explosion S4 (detonated at the site 3TY) and recorded at the collocated sensors PS05 (velocimeter) and PS05A (MEMS accelerometer). The black traces are the vertical components, the green traces are the radial components, and the orange traces are the transverse components. The origin time corresponds to the estimated origin time for the explosion S4, that is, 12 December 2018 T07:20:29.5 (see the [Inversion of onset times to better infer source locations and explosion times](#) section). The gray dashed vertical lines correspond to the approximate time arrivals of *P*, *S*, and *H* phases, respectively. The color version of this figure is available only in the electronic edition.

This denotes that the waveforms that follow the second pulse are mostly sensitive to the medium heterogeneity along the different ray paths. We do not observe this second pulse on the horizontal components of the seismograms (Fig. S2). Though, we also observe that the time delay between the first two pulses is correlated with the charge weights in phase (Fig. 8). For the five explosions S3–S7 occurring on the seabed at the site 3TY, the time delay between the two pulses is approximately 0.09 s for S3 (i.e., a charge weight of 80 kg TNT-equivalent), 0.11 s for S7 (i.e., a charge weight of 200 kg TNT-equivalent), 0.13 s for S6 (i.e., a charge weight of 400 kg TNT-equivalent), 0.14 s for S5 (i.e., a charge weight of 600 kg TNT-equivalent), and 0.15 s for S4 (i.e., a charge weight of 680 kg TNT-equivalent). For the



explosion S8, also located at the site 3TY but occurring within the water column (third trace in Fig. 8), the coherency of the waveforms seems lost just after the first pulse.

Whereas the first pulse of energy is caused by the explosion itself, the second pulse is likely due to the fact that the gas globe (often called “bubble”) generated by the explosion cannot spherically expand due to the proximity of the seabed and, consequently, quickly collapses (Plesset and Chapman, 1971). Bubble collapse is known to generate high-velocity water jets that can cause large damages to the hull of vessels in the case of an underwater explosion at short distances (e.g., Reid, 1996; Kim and Gitterman, 2013). In the case of an explosion on the seabed, and if the water jet is the cause of our observation, it seems that this process shocks the floor with even more energy than the explosion itself. Indeed, the amplitudes of the second pulse are greater than those of the first pulse. As a result, the increase in the time delay with increasing charge weight could be explained by the fact that the larger the explosion the later the bubble collapses and the later the water jet is generated (Reid, 1996). It is, however, not clear why the time delay between the two pulses is slightly smaller for the explosions S1 and S2 than for the explosion S3, though they all three correspond to the same charge weight (namely, 80 kg TNT-equivalent) and the same

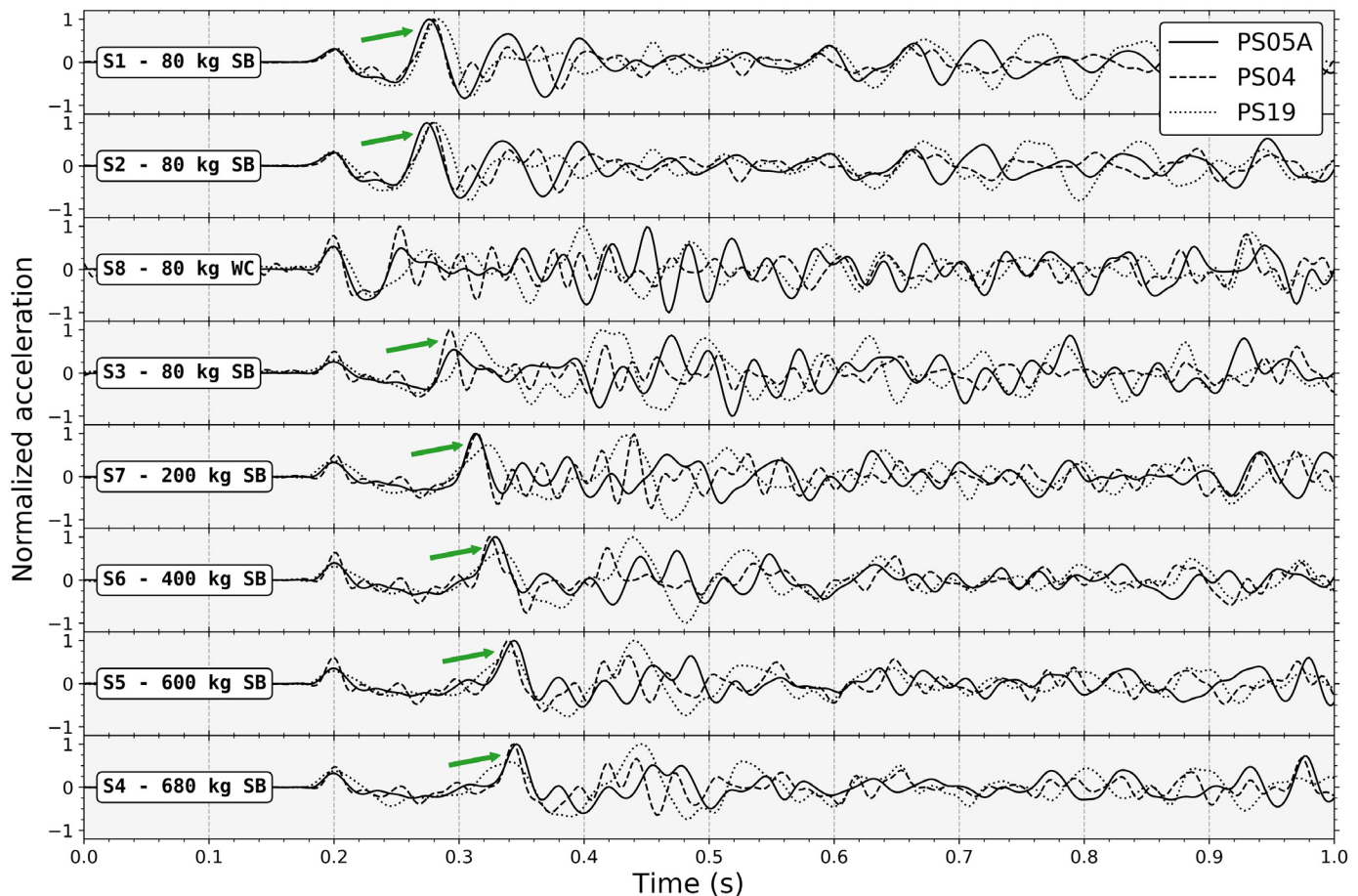
Figure 7. Spectrograms obtained from the vertical component of the signals generated by the explosion S8 (charge of 80 kg TNT-equivalent weight located at the site 3TY in the water column) and recorded by the MEMS accelerometers. The spectrograms are ordered as a function of the epicentral distances. The white solid arrows indicate the onset of the *H* phase, and the white open arrow indicates the onset of the acoustic phase (*I* phase). The spectrograms are computed over time windows of 0.2 s with 90% overlap. The color version of this figure is available only in the electronic edition.

configuration (occurring on the seabed). The water depth, the sediment thickness, the meteorological conditions or the physicochemical properties of the sea water likely have some impact on the water jet generation.

CONTRIBUTION OF THE *H* PHASE TO THE IMPROVEMENT IN SIGNAL ANALYSIS

Inversion of onset times to better infer source locations and explosion times

Seismic signals generated by underwater explosions are regularly detected by permanent networks, and routine inversions of the corresponding *P*- and *S*-wave onset times allow to locate sources and to define origin times. However, these source parameters are rarely compared to information provided by the FNMWO (if any), and one can thus wonder whether such



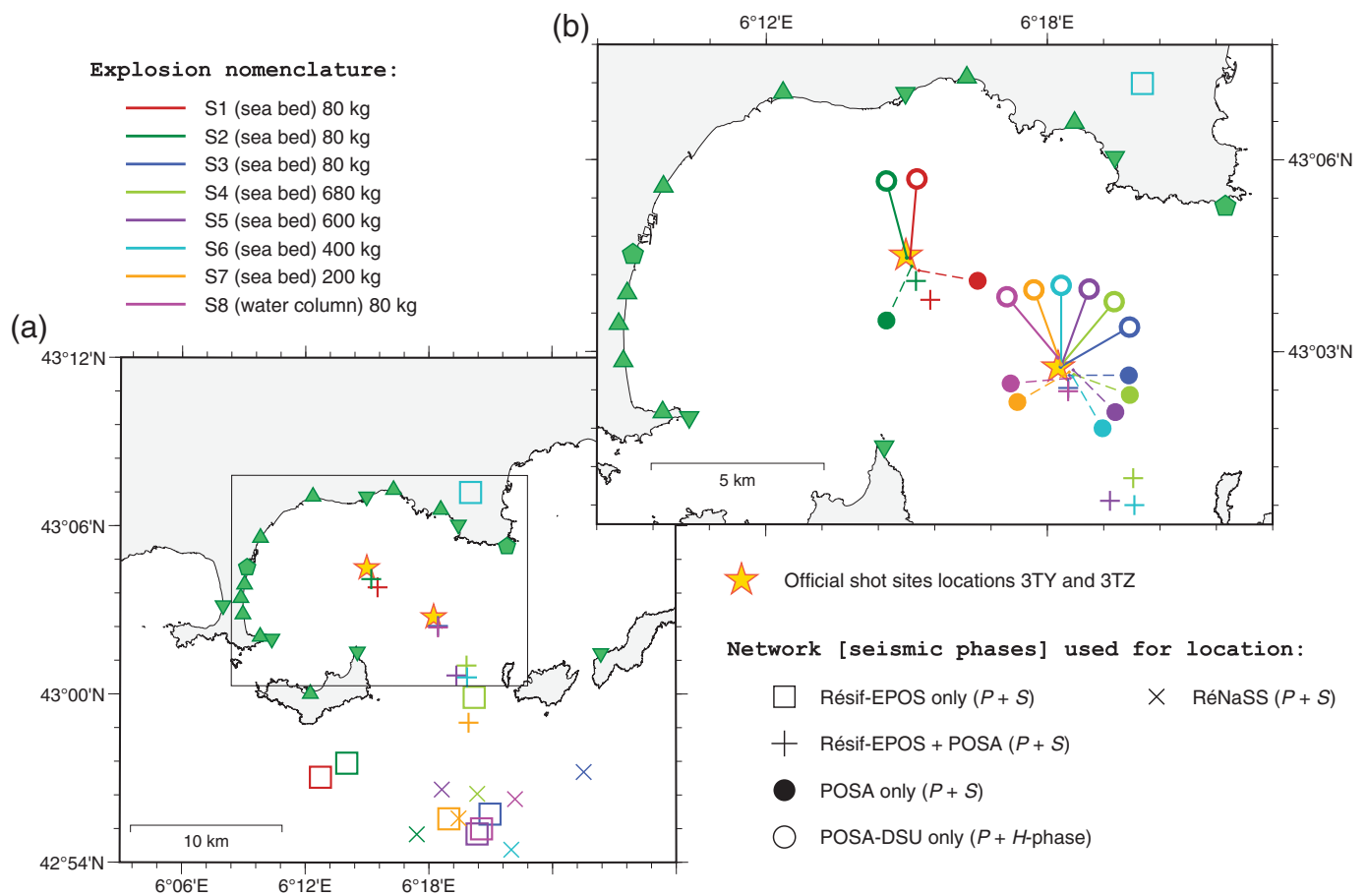
networks are fully relevant is this situation. As a result, considering the particular shape of the Bay of Hyères, the geometry of the temporary network (Fig. 1), and the experimental conditions, the POSA experiment provides a rare opportunity to constrain inversion results.

We have relied on two different inversion procedures (detailed hereafter) to infer source locations and explosion times. The first one is a classical iterative weighted linearized inversion that uses *P*- and *S*-wave onset times recorded by (1) the regional permanent broadband stations (Fig. 1a), (2) the temporary network (velocimeters and accelerometers) of the POSA experiment only, and (3) both permanent and temporary seismic stations. The second inversion scheme relies on a stochastic exploration of the parameter space that uses only *P* and *H* phases recorded by the MEMS accelerometers.

Linearized inversion using *P* and *S* phases. For each of the eight explosions, the *P*- and *S*-wave onset times are picked on all the available seismograms recorded at both permanent (Résef-EPOS) and temporary (POSA) seismic stations. Locations and origin times of the sources are obtained by the Hypocenter program embedded in SeisComp3 (Weber *et al.*, 2007), using an iterative weighted linearized inversion scheme. The IASP91 1D Earth model (Kennett and Engdahl, 1991) is used to compute body wave travel times.

Figure 8. Detail of one second of the signal that includes the *P*-wave onset (at 0.2 s) generated by the explosions S1–S2 (located at the site 3TZ) and by the explosions S3–S8 (located at the site 3TY), and recorded at the stations PS05A (solid), PS04 (dashed), and PS19 (dotted). The vertical component of the seismograms is low-pass filtered at 50 Hz, and the amplitudes are normalized. The green arrows highlight a phase whose delay seems correlated to the charge weights. The color version of this figure is available only in the electronic edition.

The first subset of inverted data corresponds to what observatories and national agencies are able to routinely record and detect using permanent seismic stations at regional epicentral distances. The locations obtained with this subset are reported in Figure 9 (open squares). They largely differ from the locations given by the FNMWO (stars in Fig. 9) but are relatively similar to those available in the bulletin of the Bureau Central de la Sismicité Française - Réseau National de Surveillance Sismique (BCSF-RéNaSS)—the academic French agency responsible for the location of the earthquakes in metropolitan France (crosses in Fig. 9a). We may notice that an ad hoc velocity model (Cara *et al.*, 2015) is used by the BCSF-RéNaSS to locate events in this region. The mean epicentral distance between the known locations and those from our inversions is $\delta_1 = 12.2 \pm 2.95$ km. More importantly, the inferred locations exhibit a systematic southward offset at first order due to the poor back-azimuthal



coverage of the Résif-EPOS network (no instrument on the sea side) and, to a lesser extent, to the relatively poor knowledge of the crustal seismic velocities in the region.

When adding the picked arrival times estimated from the data recorded by the temporary POSA network (plus signs in Fig. 9), the mean epicentral distance between the known locations and those from the inversions is largely reduced, namely $\delta_2 = 2.94 \pm 2.26$ km. However, the standard deviation is of the same order as the mean value, which is indicative of a largely unstable behavior of the inversion. Counter intuitively, the largest mislocations (as large as 7.3 km) are measured for the largest explosions (S5–S7). This is largely due to the fact that the picked arrival times from the regional permanent stations dominate the dataset for these large events.

Finally, when considering the picked arrival times estimated from the data recorded by the POSA network only (solid circles in Fig. 9b), the locations are dramatically improved, that is, $\delta_3 = 0.45 \pm 0.074$ km. This can be explained by the fact that (1) the picking of the seismic phase onsets (especially for S waves) is more reliable at short epicentral distances, and (2) a 1D Earth model is more representative of a small Earth volume, regardless of its link to real local geological features.

Bayesian inferences using P and H phases. The second inversion procedure is based on parallelized nonlinear

Figure 9. Estimated locations of the eight explosions using different inversion strategies. (a) The locations denoted by the squares were obtained from the time arrivals at the regional permanent stations only, whereas the plus signs also use data from the local POSA experiment. The locations denoted by the crosses are the location available in the bulletin of the BCSF-RéNaSS and computed using only P - and S -arrival times. (b) The solid circles show the locations obtained using only the local POSA experiment. The open circles show the locations obtained from the MEMS accelerometers only, considering the P - and H -wave arrival times, whereas the green solid symbols denote the locations of the temporary stations of the POSA experiment. The symbols used for the stations are the same as in Figure 1.

explorations of a parameter space using Monte Carlo Markov chain (Haugmard, 2016), jointly with the picking of the P - and H -phases arrival times. This approach is only possible with the MEMS accelerometers that were able to fully record the H phase (Fig. 6). The inversion procedure samples an eight-dimension parameter space to determine the posterior distributions of four sources parameters (i.e., latitude, longitude, depth, and origin time), as well as four medium properties (V_P in the first layer, V_P in the second layer, velocity ratio V_P/V_H of the two picked phases [here, P and H phases], and interface depth), for a simple two-layered 1D model. Although this inversion scheme is originally designed to decrease the weight of a priori model in regions where velocities are not well constrained (such

TABLE 3

Explosion Location and Ignition Times Using the *H*-Phase Phase and a Nonlinear Inverse Method

ID	Lat. (°)	Lon. (°)	Depth (km)	V_P (km/s)	V_H (km/s)	t_0 (UTC)
S1	43.0745	6.2513	0.09	4.73	1.517	2018-345T13:13:29.57
S2	43.0745	6.2502	0.08	4.88	1.533	2018-345T14:03:03.75
S3	43.0462	6.3046	0.11	4.67	1.517	2018-345T15:28:20.53
S4	43.0472	6.3055	0.09	4.86	1.518	2018-346T07:20:29.25
S5	43.0469	6.3053	0.09	4.85	1.514	2018-346T08:10:44.42
S6	43.0467	6.3049	0.09	4.87	1.527	2018-346T09:03:19.97
S7	43.0467	6.3049	0.09	4.79	1.513	2018-346T09:48:35.27
S8	43.0486	6.3038	0.09	4.95	1.543	2018-346T12:37:50.93

V_H is obtained from the posterior distribution of the V_P/V_H ratio. Lat., latitude; lon., longitude; and t_0 , origin time of the explosion.

as in the cases of postseismic campaigns), it can be used in the context of the POSA experiment.

Because the chosen parametrization is an infinite half-space overlaid by a low-velocity layer, we make here the simplistic assumption that *P* waves and *H* phases propagate in the same layer (we impose no water layer) and along the same ray path. This means that we are looking for an effective velocity model that is not necessarily geologically meaningful, but that gives the best fit to the data set. Indeed, by choosing large priors for V_P and V_H (namely, between 0.5 and 5 km s⁻¹), the efficient explorations of the model parameters that rely on a Metropolis–Hastings acceptance and rejection algorithm (Hastings, 1970) rapidly converge toward the values of 4.8 km s⁻¹ and 1.5 km s⁻¹ for V_P and V_H , respectively. As seen in Figure 9b (open circles), the inferred locations match very well with the locations indicated by the FNMWO operators, the mean epicentral distance between the locations now being $\delta_4 = 0.16 \pm 0.069$ km. Inverted source depths are also consistent with the ground truth (depth close to 100 m). However, the explosion S8 occurring in the water column cannot be discriminated from the other explosions occurring on the seabed. The hypocenter parameters determined from this inversion scheme are summarized in Table 3.

Frequency content of the explosion-induced seismic signals as a function of the charge weight

Figure 10 shows the power spectral densities (PSDs) of the vertical component of the ground accelerations recorded at the station PS05A (corresponding to a MEMS accelerometer at the location PS05) and induced by the detonations at the explosion site 3TY (Fig. 1b). The curves correspond to the median of the PSD computed in frequency bins of one-third of octave.

We see that below 0.5 Hz and whatever the charge weight all the PSD are of the same magnitude, and the curves follow the same linear trend. This corresponds to the self-noise of the MEMS accelerometers below 1 Hz (see Figs. S3 and S4). In the frequency range where the MEMS accelerometers are sensitive, the most striking pattern is that the explosions with a charge weight larger than 80 kg TNT-equivalent generate a

similar spectral response: a first energy “peak” around 1 Hz, a decrease in the amplitude between 2 and 5 Hz followed, around 7 Hz, by the largest amplitudes. The energy then linearly decreases as the frequency increases to reach 100 Hz where a last energy “peak” appears. For charge weights above 200 kg TNT-equivalent, the amplitude ratio of the low-frequency part of the spectra is consistent with the charge weight ratio (difference of 5 dB, i.e., a factor two in amplitude, for instance between the explosions S6 and S7 at 1 Hz).

For the *H* phase (peak around 100 Hz), the linearity between the charge weight and the PSD amplitude is no longer preserved. For instance, the explosion S5 corresponding to a charge weight of 600 kg TNT-equivalent is more energetic than the explosion S4 corresponding to a charge weight of 680 kg TNT-equivalent. A comparison of the spectra generated by the explosions S3 and S8, both corresponding to a charge weight of 80 kg TNT-equivalent, but on the seafloor and in the water column, respectively, shows that, as expected, an explosion within the water column dramatically limits the release of seismic energy between 1 and 10 Hz. This is consequently associated with a lower magnitude estimation from the regional networks (Favretto-Cristini, Garlan, *et al.*, 2022). In contrast, the 80 kg TNT-equivalent charge weight explosion in the water column generates an *H* phase as energetic as the explosion S6 (400 kg TNT-equivalent weight) and thus releases dramatically more energy in the water than an explosion of a 80 kg TNT-equivalent charge weight located on the seabed (approximately a difference of 10 dB with respect to the explosion S3). This observation is of primary importance for the mitigation of the noise nuisances generated by UXO disposal, especially for sea fauna.

GROUND RESPONSE TO THE EXPLOSION-INDUCED SEISMIC MOTION

Influence of the surface geology on the explosion-induced seismic motion

As shown earlier (see also Favretto-Cristini, Garlan, *et al.*, 2022), the waveforms and signal durations greatly differ according to the explosion–station distances and to the ground properties along the propagation path. In particular, the

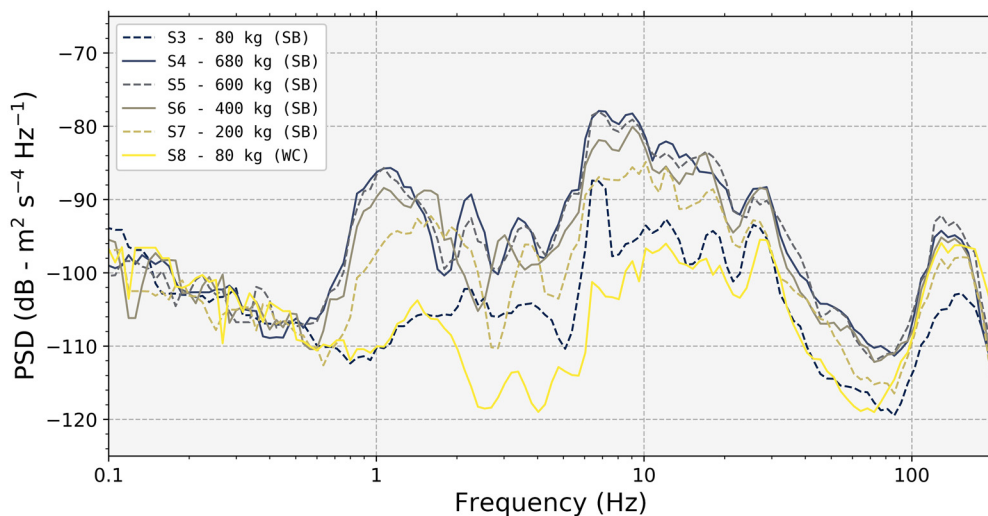


Figure 10. Power spectral densities of the seismic signals recorded at the station PS05A (vertical component) and induced by the explosions S3–S8 at the site 3TY. SB and WC refer to the configuration of the explosions, namely on the sea bottom and in the water column, respectively. The color version of this figure is available only in the electronic edition.

sediment thickness along the path seems to have a significant influence (Favretto-Cristini, Wang, *et al.*, 2022). For example, the *P*-wave arrival is less impulsive at sites with a significant sedimentary thickness (see the sites PS09–PS16). More importantly, the signal duration is much longer with the presence of late dispersive signals with a clear low-frequency content (1–10 Hz) and relatively large amplitudes (Fig. 4).

To highlight the effect of the surface geology on the signal characteristics, we carry out, in a first step, a classical microtremor horizontal-to-vertical spectral ratio (mHVSR) analysis of one-hour of continuous seismic signal recorded at all the stations (Fig. 11). The frequency peaks from the mHVSR curves are known to be related to the first resonance frequency of the site, what is known as the lithological site effect (Nakamura, 1989; Lermo and Chávez-García, 1993; Sánchez-Sesma *et al.*, 2011). In our case, a peak around 1–3 Hz can be clearly seen at the stations where the sediment layer is relatively thick (namely, 15–30 m), that is, along the tombolo of the Giens Peninsula (stations PS10, PS12, PS15, and PS16). On the other hand, rather flat mHVSR curves can be seen for all the stations located at the northern part of the Bay of Hyères and on the islands (stations PS03, PS04, PS05, PS18, and PS19) where the sedimentary thickness is less than 5 m (see Fig. 2). Higher frequency peaks (>5 Hz) are present at some stations, and these peaks are probably related to superficial muddy or sandy layers present at the sites (e.g., PS06 or PS08).

In addition, we calculate the earthquake horizontal-to-vertical spectral ratio (eHVSR) of all the explosion-induced signals at each site using the whole signal (time windows of 60 s). This technique is widely used in earthquake engineering as a proxy for site amplification, especially when it is difficult to

define (or in the absence of) a reference station (Kawase *et al.*, 2011). The results shown in Figure 11 match quite well the mHVSR curves for all the sites and for the whole frequency range of interest. Two main conclusions can thus be drawn: (1) the relevance of the lithological site effect on ground motions recorded at the nearby coastal areas for the particular case of underwater explosions, and (2) the fact that the recorded signals are mainly composed of surface waves whose energy is amplified (or not) at each station depending on the site characteristics (similarly to mHVSR).

Impact on one medium-size masonry structure located on land

The station PS01-PS01H is composed of two medium-band velocimeters. One (PS01H) is located at the top of the bell tower of the Saint Anne church in the center of the Porquerolles village, whereas the other (PS01) is located 12 m below (i.e., at the ground level) inside the church. The purpose of this specific experiment is to evaluate the impact of underwater explosions on nearby engineering structures. Figure 12a,b illustrates the north-component acceleration traces at the stations PS01 and PS01H for the explosion S5 from where it can be clearly seen the motion amplification due to the structure. The peak ground acceleration (PGA), peak ground velocity (PGV), and peak ground displacement (PGD) are extracted from the seismograms after careful instrumental response correction and integration procedures (Boore, 1989). PGA values around $2.0 \times 10^{-2} \text{ m s}^{-2}$ are obtained for the largest charges (S4 and S5) at the top of the bell tower (see Fig. 12b). For these explosions, PGV reach values around $0.4 \times 10^{-3} \text{ m s}^{-2}$ at the top (Fig. 12c), therefore slightly higher than the limit of human perception of vibrations (i.e., $0.1\text{--}0.3 \times 10^{-3} \text{ m s}^{-1}$). However, PGD values less than $1.0 \times 10^{-5} \text{ m}$, estimated from the recordings (Fig. 12d), are well below the damage initiation threshold assumed for typical masonry structures (D’Ayala, 2013; Lagomarsino and Cattari, 2015).

After rotation of the horizontal components of the seismograms to obtain transverse (N20°E) and longitudinal (N110°E) directions with respect to the main structure (i.e., the nave of the church), classical spectral analysis (namely, Fourier spectra and transfer functions—spectral ratios between the top and the bottom of the bell tower, respectively) was carried out to

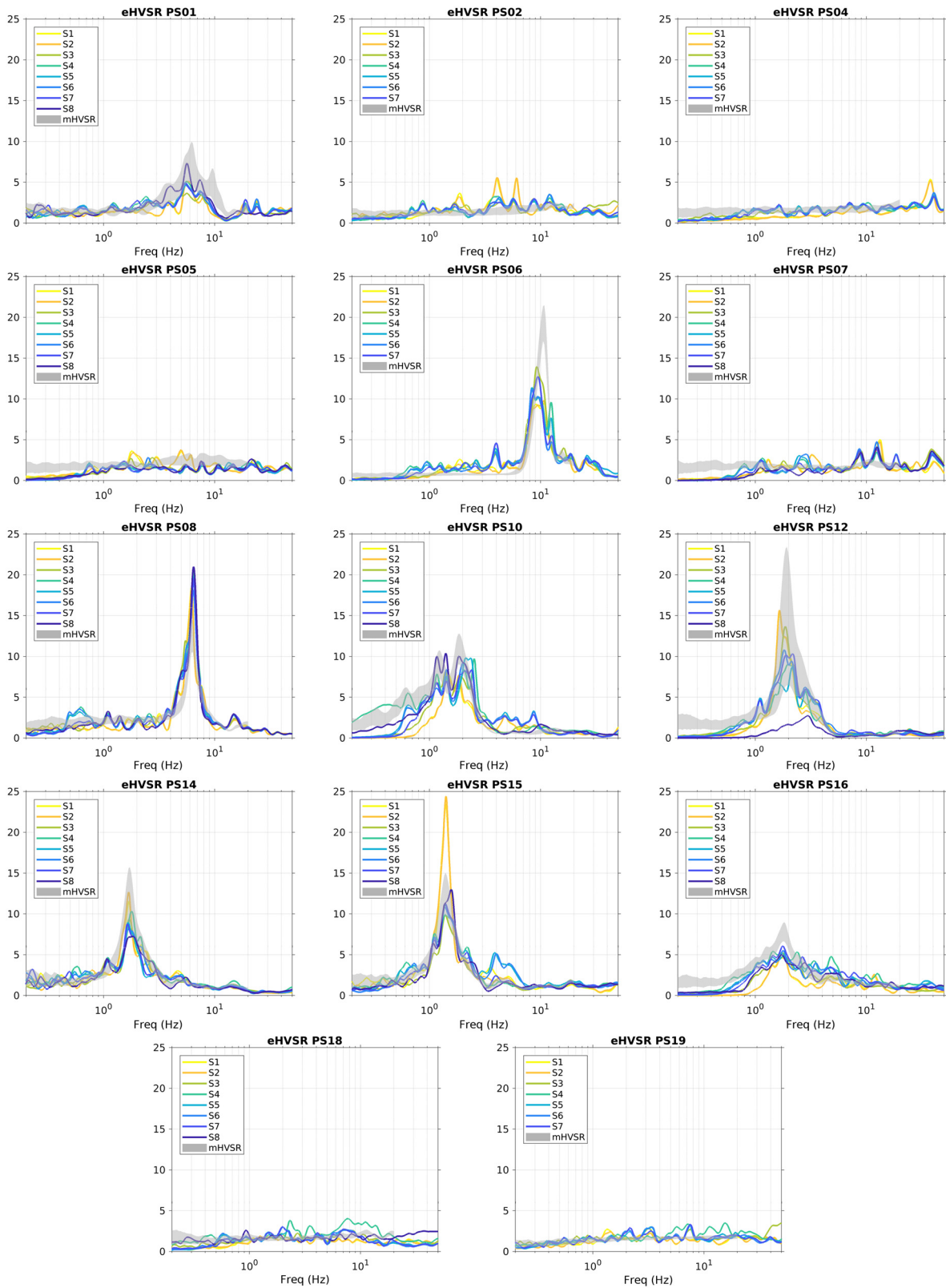


Figure 11. Earthquake horizontal over vertical spectral ratio (eHVSr, from the signals generated by the eight detonations) and microseismic HVSr (mHVSr, from the continuous seismic signal) computed at 13 stations of the

POSA experiment. Note the correlation between eHVSr and mHVSr at all the sites, and the variability of the soil response along the Bay of Hyères. The color version of this figure is available only in the electronic edition.

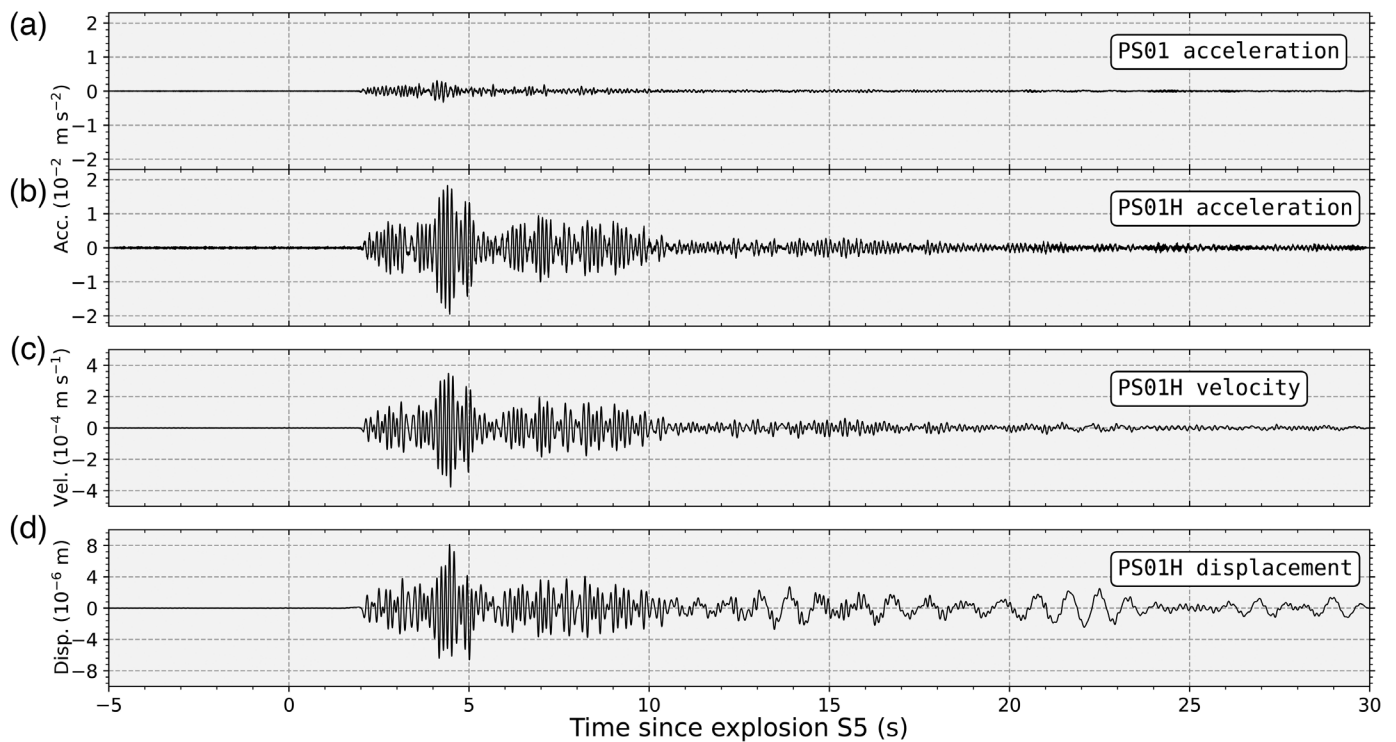


Figure 12. Comparison of the seismic signals (transverse component of the seismograms) at the station PS01 (floor of the church) and the station PS01H (bell tower) for the explosion S5 (charge weight of 600 kg TNT-equivalent). (a) Acceleration of the ground at PS01 and (b) acceleration of the structure at PS01H. Note the amplification of the motion between the floor and the bell tower. (c) Velocity of the ground at the station PS01H and (d) displacement of the structure at the station PS01H.

estimate the normal modes of vibration and to compare the building response for different explosive charges. Several interesting features can be highlighted from Figure 13. First, from the transfer functions, structural modes are clearly identified at 6.1, 8.5, and 9.7 Hz in the transverse direction and 6.6 and 9.7 Hz in the longitudinal direction. Higher modes can also be seen for frequencies above 20 Hz. Second, these modes do not seem to be significantly modified by the differences in explosive weight, though some slight shift in the frequency peaks (between 1% and 2%) can be observed for some modes for the explosions S4–S7, suggesting the onset of the nonlinear response of the structure (see insets around fundamental modes in Fig. 13). Further analysis of these features is work in progress.

CONCLUSION

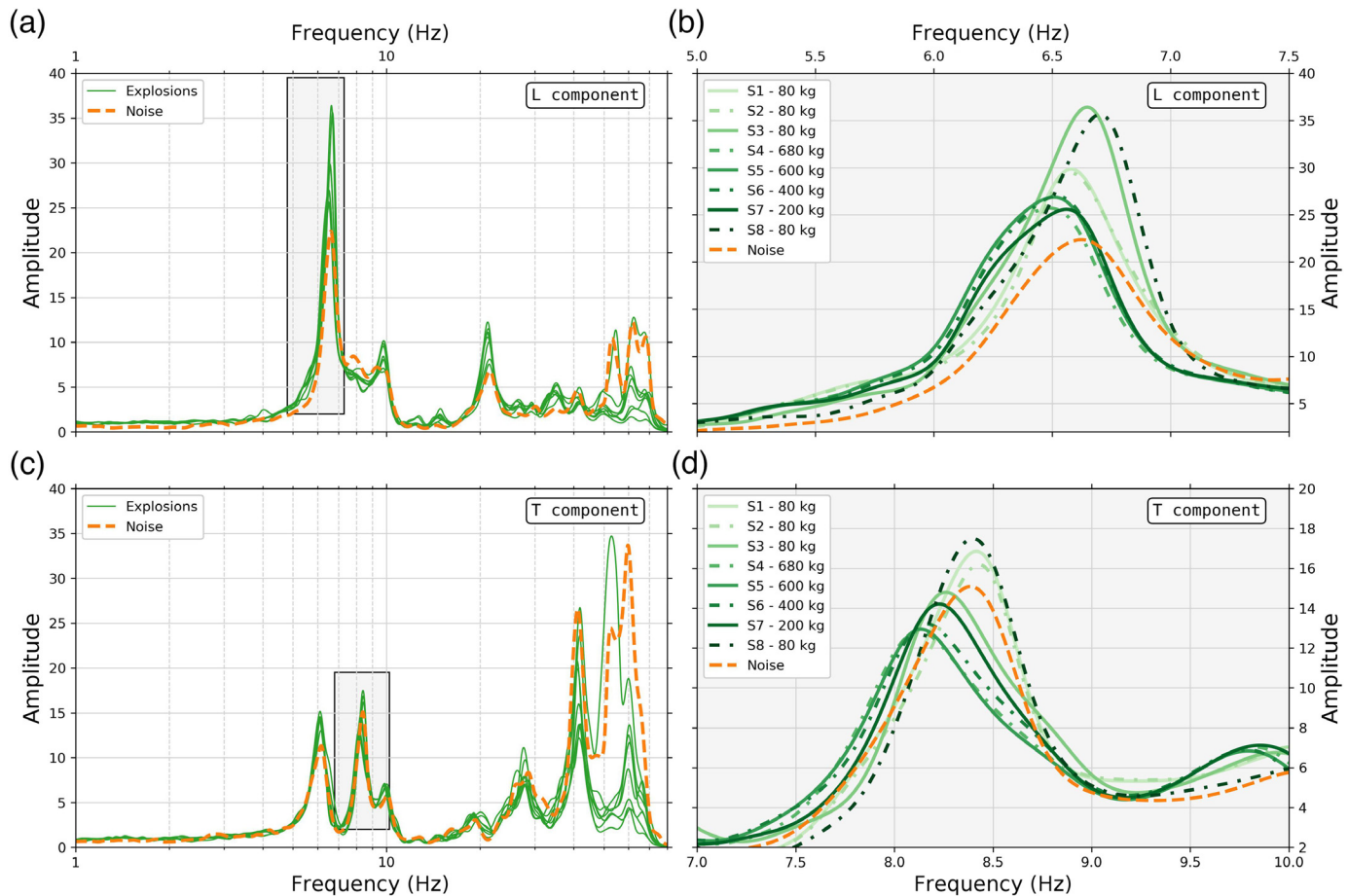
We study the effects on the shore of UXO disposal in a shallow water environment using a seismic dataset obtained during the POSA experiment conducted in December 2018. The dataset comprises records of eight explosions with charge weight ranging from 80 to 680 kg TNT-equivalent. The originality of this work relies in the fact that the dataset is composed of both data recorded by the French permanent network (whose stations are located at several tens of kilometers from the explosion sites) and data recorded by 17 temporary seismic stations deployed in the Bay of Hyères (France). The temporary network was composed of conventional medium and broadband sensors (accelerometers and velocimeters) and MEMS accelerometers.

The use of relatively high sampling rates (250 and 500 samples per second) allows to record high amplitude *H* phase that corresponds to acoustic energy converted to seismic energy at the shore. This energy faces low attenuation and is mostly

observed at the rocky sites where the bathymetry is relatively steep. As the *H*-phase signals are the most energetic ones recorded during the experiment, we suggest that these phases might play an important role in the human perception of UXO disposal near the shore. The use of the *H*-phase arrival times also allows us to locate more accurately the explosions at about a distance of 100 m from the official location given by the French Navy.

When looking at the first tenths of seconds after the onset on the *P* wave, we notice that a second pulse that is consistent in phase and amplitude ratio at many stations is observed for this configuration. We propose that this pulse whose delay with respect to the *P*-wave onset is correlated with charge weights is generated by a water jet generated by the rapid collapse of the gas globe due to its interaction with the seabed. This observation has, to our knowledge, never been made before.

Spectral analyzes of the seismic signals induced by the eight explosions at a each station indicate that the explosion configuration (seabed or water column) has a dramatic effect on the frequency content of the seismic signal received at the shore. In particular, the explosions within the water column radiate



significantly less energy in the 1–10 Hz frequency range compared to the explosions of equivalent charge weights occurring on the seabed. In contrast, the amplitude of the *H* phase generated by the explosion of a charge weight of 80 kg TNT-equivalent in a water column configuration is equivalent to the amplitude of the *H* phase generated by a charge weight of 400 kg TNT-equivalent. Given the fact that an explosion within the water column releases more energy in the water, it may cause dramatic nuisances for the aquatic wildlife. Minimizing seismic risk on the shore by counterming in the water column rather than on the seabed should thus be more carefully investigated, especially when considering that a single explosion was triggered in the water column during the experiment.

Use of mHVSr and eHVSr shows the importance of the sedimentary cover on the frequency content of the seismic signal recorded on land. Thick sediment layers (as along the tombolo of the Giens Peninsula) are associated with important seismic amplifications (horizontal-to-vertical ratio up to 20) of the relatively low-frequency energy (1–5 Hz). This evidences that the sedimentary cover has to be taken into account to mitigate potential nuisance on land for large-charge weights in shallow water environments. Finally, we compare the seismic signal at the top and the bottom of the Saint Anne bell tower on the Porquerolles Island. It evidences that this masonry structure faces motion amplification in response to the explosion-

Figure 13. Transfer functions of the Sainte-Anne church to the solicitations of seismic waves generated by the unexploded historical ordnance (UXO) detonation (green curves) and by the environmental seismic noise (orange curves). (a,b) Transfer functions along the longitudinal direction (along the nave of the church) and (c,d) along the transverse direction. (a,c) Transfer functions between 1 and 50 Hz. The grayed rectangles correspond to the extent of the panels on the right. (b,d) Zoom on the single peak where the nonlinear response of the building can be illustrated. The position of the peaks with respect to the full transfer function is indicated by the boxes on the left panels. The color version of this figure is available only in the electronic edition.

induced seismic signal, but that deformation is well beyond the damage initiation threshold, even for the largest charge used in the current POSA experiment.

DATA AND RESOURCES

The Résif-EPOS data (RESIF, 1995) used in the work presented here can be downloaded from the webservices through <https://seismology.resif.fr>, under the network code FR and RD (station FLAF). Data from the POSA experiment are distributed through the Résif-EPOS webservices (<https://seismology.resif.fr>) under the network code ZH (Deschamps and Beucler, 2013). Figures were produced with Generic Mapping Tools (GMT; Wessel *et al.*, 2019) and Matplotlib (Hunter and Geers, 2004). ObsPy (Krischer *et al.*, 2015), NumPy (Harris *et al.*, 2020), and Seismic Analysis Code (SAC; Goldstein and Snoke, 2005) were used to handle

and process seismic data. We have used the `read_segd` library provided by C. Satriano (https://github.com/claودیods/rd_segd) to convert SEG-D data from the DSU-428 to the miniSEED format. The supplemental material attached to this document contains (1) a figure (Fig. S1) that presents the horizontal components of the seismograms shown in Figure 4, (2) a figure (Fig. S2) that presents the acoustic signal recorded at the site PS02 for explosions S3–S8, and (3) a description of the instrumental response of the three types of instruments used in this study associated with a comparison of the continuous seismic energy recorded by the three types of sensors at the site PS05-PS05A (Figs. S3 and S4).

DECLARATION OF COMPETING INTERESTS

The authors acknowledge that there are no conflicts of interest recorded.

ACKNOWLEDGMENTS

The authors thank the two anonymous reviewers for their valuable comments that helped to improve the article. Research presented in this article was part of the POSA program and supported by The French National Research Agency (ANR) and cofunded by DGA (French Ministry of Defense Procurement Agency) under reference Projet ANR-15-ASTR-0001 POSA. This work was granted access to the seismic resources of Résif-EPOS. Résif-EPOS is a Research Infrastructure (RI) managed by Centre National de la Recherche Scientifique (CNRS-Insu). Inscribed on the roadmap of the Ministry of Higher Education, Research, and Innovation, the Résif-EPOS IR is a consortium of 18 French research organizations and institutions. Résif-EPOS benefits from the support of the Ministry of Ecological Transition. The authors greatly acknowledge the Préfecture de la Méditerranée, the Groupe des Plongeurs Démineurs (GPD), and the Force de Guerre des Mines for their management of the two countermining operations. Shom, and, in particular, X. Mathias, P. Guyomard, E. Brenon, H. Gauduin, M. Gosselin, J. P. Boivin, and F. Jourdin are acknowledged for the hydrographic and geological surveys. X. Martin and J. Chèze (Géoazur), M. Pernoud, Ph. Langlaude (Cerema), and M. Perrault (Cerema, now at Sercel S. A.) are also acknowledged for the seismic surveys. C. Maron (Géoazur) is acknowledged for the generation of the metadata of the POSA experiment.

REFERENCES

Boore, D. M. (1989). Quantitative ground-motion estimates, in *Earthquake Hazards and the Design of Constructed Facilities in the Eastern United States*, K. H. Jacob and C. J. Turkstra (Editors), Vol. 558, Annals of the New York Academy of Sciences, Wiley, 81–94.

Bormann, P., D. A. Storchak, and J. Schweitzer (2013). The IASPEI standard nomenclature of seismic phases, Deutsches GeoForschungs Zentrum GFZ, doi: [10.2312/GFZ.NMSOP-2_IS_2.1](https://doi.org/10.2312/GFZ.NMSOP-2_IS_2.1).

Bottero, A., P. Cristini, and D. Komatitsch (2020). On the influence of slopes, source, seabed and water column properties on T waves: Generation at shore, *Pure Appl. Geophys.* **177**, no. 12, 5695–5711, doi: [10.1007/s00024-020-02611-z](https://doi.org/10.1007/s00024-020-02611-z).

Buehler, J. S., and P. M. Shearer (2015). T-phase observations in global seismogram stacks, *Geophys. Res. Lett.* **42**, no. 16, 6607–6613, doi: [10.1002/2015GL064721](https://doi.org/10.1002/2015GL064721).

Cara, M., Y. Cansi, A. Schlupp, P. Arroucau, N. Béthoux, É. Beucler, S. Bruno, M. Calvet, S. Chevrot, A. Deboissy, *et al.* (2015). SI-Hex: A new catalogue of instrumental seismicity for metropolitan France, *Bull. Soc. Géol. France* **186**, no. 1, 3–19, doi: [10.2113/gssgfbull.186.1.3](https://doi.org/10.2113/gssgfbull.186.1.3).

Chantraine, J., A. Autran, and C. Cavelier (2003). Carte géologique de la France (version numérique), *Rept. BRGM*, BRGM, Orléans, France.

Chapman, N. R. (1985). Measurement of the waveform parameters of shallow explosive charges, *J. Acoust. Soc. Am.* **78**, no. 2, 672–681, doi: [10.1121/1.392436](https://doi.org/10.1121/1.392436).

Cole, R. H. (1948). *Underwater Explosion*, Princeton University Press, Princeton, New Jersey.

D’Ayala, D. F. (2013). Assessing the seismic vulnerability of masonry buildings, in *Handbook of Seismic Risk Analysis and Management of Civil Infrastructure Systems*, S. Tesfamariam and K. Goda (Editors), Woodhead Publishing, Cambridge, United Kingdom, 334–365, doi: [10.1533/9780857098986.3.334](https://doi.org/10.1533/9780857098986.3.334).

Deschamps, A., and É. Beucler (2013). POSA experiment, *RESIF—Réseau Sismologique et géodésique Français*, doi: [10.15778/RESIF.ZH2016](https://doi.org/10.15778/RESIF.ZH2016).

Favretto-Cristini, N., T. Garlan, O. Morio, X. Demoulin, M. Arrigoni, A. Deschamps, M. Bonnin, É. Beucler, E. D. Mercerat, D. Ambrois, *et al.* (2022). Assessment of risks induced by countermining unexploded large-charge historical ordnance in a shallow water environment—Part I: Real case study, *IEEE J. Ocean. Eng.* **47**, no. 2, 350–373, doi: [10.1109/joe.2021.3111819](https://doi.org/10.1109/joe.2021.3111819).

Favretto-Cristini, N., F. Wang, P. Cristini, T. Garlan, O. Morio, D. Mercerat, V. Monteiller, A. Deschamps, and É. Beucler (2022). Assessment of risks induced by countermining unexploded large-charge historical ordnance in a shallow water environment—Part II: Modeling of seismo-acoustic wave propagation, *IEEE J. Ocean. Eng.* **47**, no. 2, 374–398, doi: [10.1109/joe.2021.3111791](https://doi.org/10.1109/joe.2021.3111791).

Gitterman, Y., and L. D. Sadwin (2017). Blast wave observations for large-scale underwater explosions in the Dead Sea, *30th International Symposium on Shock Waves*, Springer International Publishing, 1315–1319, doi: [10.1007/978-3-319-44866-4_91](https://doi.org/10.1007/978-3-319-44866-4_91).

Goldstein, P., and A. Snoke (2005). SAC availability for the IRIS community, *Tech. Rept.*, available at <http://ds.iris.edu/ds/newsletter/vol7/no1/> (last accessed October 2022).

Harris, C. R., K. J. Millman, S. J. van der Walt, R. Gommers, P. Virtanen, D. Cournapeau, E. Wieser, J. Taylor, S. Berg, N. J. Smith, *et al.* (2020). Array programming with NumPy, *Nature* **585**, no. 7825, 357–362, doi: [10.1038/s41586-020-2649-2](https://doi.org/10.1038/s41586-020-2649-2).

Hastings, W. (1970). Monte-carlo sampling methods using markov chains and their applications, *Biometrika* **57**, no. 1, 97–109, doi: [10.2307/2334940](https://doi.org/10.2307/2334940).

Haugmard, M. (2016). Détermination non-linéaire des paramètres hypocentraux et structuraux: Application à la sismicité intracontinentale du Massif armoricain, *Ph.D. Thesis*, Université de Nantes (in French).

Heyburn, R., S. E. J. Nippres, and D. Bowers (2018). Seismic and hydroacoustic observations from underwater explosions off the East coast of Florida, *Bull. Seismol. Soc. Am.* **108**, no. 6, 3612–3624, doi: [10.1785/0120180105](https://doi.org/10.1785/0120180105).

Hunter, K. S., and T. L. Geers (2004). Pressure and velocity fields produced by an underwater explosion, *J. Acoust. Soc. Am.* **115**, no. 4, 1483–1496, doi: [10.1121/1.1648680](https://doi.org/10.1121/1.1648680).

Johnson, R. H., J. Northrop, and R. Eppley (1963). Sources of Pacific T phases, *J. Geophys. Res.* **68**, no. 14, 4251–4260, doi: [10.1029/JZ068i014p04251](https://doi.org/10.1029/JZ068i014p04251).

Kawase, H., F. J. Sánchez-Sesma, and S. Matsushima (2011). The optimal use of horizontal-to-vertical spectral ratios of earthquake motions for velocity inversions based on diffuse-field theory for

- plane waves, *Bull. Seismol. Soc. Am.* **101**, no. 5, 2001–2014, doi: [10.1785/0120100263](https://doi.org/10.1785/0120100263).
- Kennett, B. L. N., and E. R. Engdahl (1991). Traveltimes for global earthquake location and phase identification, *Geophys. J. Int.* **105**, no. 2, 429–465, doi: [10.1111/j.1365-246X.1991.tb06724.x](https://doi.org/10.1111/j.1365-246X.1991.tb06724.x).
- Kim, S. G., and Y. Gitterman (2013). Underwater explosion (UWE) analysis of the ROKS Cheonan incident, *Pure Appl. Geophys.* **170**, 547–560, doi: [10.1007/s00024-012-0554-9](https://doi.org/10.1007/s00024-012-0554-9).
- Krischer, L., T. Megies, R. Barsch, M. Beyreuther, T. Lecocq, C. Caudron, and J. Wassermann (2015). ObsPy: A bridge for seismology into the scientific Python ecosystem, *Comput. Sci. Discov.* **8**, 014003, doi: [10.1088/1749-4699/8/1/014003](https://doi.org/10.1088/1749-4699/8/1/014003).
- Lagomarsino, S., and S. Cattari (2015). PERPETUATE guidelines for seismic performance-based assessment of cultural heritage masonry structures, *Bull. Earthq. Eng.* **13**, no. 1, 13–47, doi: [10.1007/s10518-014-9674-1](https://doi.org/10.1007/s10518-014-9674-1).
- Larroque, C., S. Baize, J. Albaric, H. Jomard, J. Trévisan, M. Godano, M. Cushing, A. Deschamps, C. Sue, B. Delouis, *et al.* (2022). Seismotectonics of southeast France: From the Jura Mountains to Corsica, *C. R. Géosci.* **353**, no. S1, 105–151, doi: [10.5802/crgeos.69](https://doi.org/10.5802/crgeos.69).
- Lermo, J., and F. J. Chávez-García (1993). Site effect evaluation using spectral ratios with only one station, *Bull. Seismol. Soc. Am.* **83**, no. 5, 1574–1594, doi: [10.1785/BSSA0830051574](https://doi.org/10.1785/BSSA0830051574).
- Nakamura, Y. (1989). A method for dynamic characteristics estimation of subsurface using microtremor on the ground surface, *Railway Technical Research Institute, Quarterly Rept.*, 25–33.
- Nolet, G., and L. M. Dorman (1996). Waveform analysis of Scholte modes in ocean sediment layers, *Geophys. J. Int.* **125**, no. 2, 385–396, doi: [10.1111/j.1365-246x.1996.tb00006.x](https://doi.org/10.1111/j.1365-246x.1996.tb00006.x).
- Plesset, M. S., and R. B. Chapman (1971). Collapse of an initial spherical vapour cavity in the neighborhood of a solid boundary, *J. Fluid Mech.* **47**, no. 2, doi: [10.1017/S0022112071001058](https://doi.org/10.1017/S0022112071001058).
- Reid, W. D. (1996). The response of surface ships to underwater explosions, *Report DSTO-GD-0109*, Defense Science and Technology Organisation.
- RESIF (1995). RESIF-RLBP French Broad-band network, RESIF-RAP strong motion network and other seismic stations in metropolitan France, *RESIF—Réseau Sismologique et géodésique Français*, doi: [10.15778/RESIF.FR](https://doi.org/10.15778/RESIF.FR).
- Salomons, E. M., B. Binnerts, K. Betke, and A. M. von Benda-Beckmann (2021). Noise of underwater explosions in the North Sea. A comparison of experimental data and model predictions, *J. Acoust. Soc. Am.* **149**, no. 3, 1878–1888, doi: [10.1121/10.0003754](https://doi.org/10.1121/10.0003754).
- Sánchez-Sesma, F. J., M. Rodríguez, U. Iturrarán-Viveros, F. Luzón, M. Campillo, L. Margerin, A. García-Jerez, M. Suarez, M. A. Santoyo, and A. Rodríguez-Castellanos (2011). A theory for microtremor H/V spectral ratio: Application for a layered medium, *Geophys. J. Int.* **186**, no. 1, 221–225, doi: [10.1111/j.1365-246X.2011.05064.x](https://doi.org/10.1111/j.1365-246X.2011.05064.x).
- Soloway, A. G., and P. H. Dahl (2014). Peak sound pressure and sound exposure level from underwater explosions in shallow water, *J. Acoust. Soc. Am.* **136**, no. 3, EL218–EL223, doi: [10.1121/1.4892668](https://doi.org/10.1121/1.4892668).
- Talandier, J., and E. A. Okal (1998). On the mechanism of conversion of seismic waves to and from *T* waves in the vicinity of island shores, *Bull. Seismol. Soc. Am.* **88**, no. 2, 621–632, doi: [10.1785/BSSA0880020621](https://doi.org/10.1785/BSSA0880020621).
- von Benda-Beckmann, A. M., G. Aarts, H. O. Sertlek, K. Lucke, W. C. Verboom, R. A. Kastelein, D. R. Ketten, R. Bemmelen, F.-P. A. Lam, R. J. Kirkwood, *et al.* (2015). Assessing the impact of underwater clearance of unexploded ordnance on harbour porpoises (*Phocoena phocoena*) in the southern North Sea, *Aquat. Mamm.* **41**, no. 4, 503–523, doi: [10.1578/am.41.4.2015.503](https://doi.org/10.1578/am.41.4.2015.503).
- Weber, B., J. Becker, W. Hanka, A. Heinloo, M. Hoffmann, T. Kraft, D. Pahlke, J. Reinhardt, J. Saul, and H. Thoms (2007). Seiscomp3—automatic and interactive real time data processing, *Geophysical Research Abstracts*, Vol. 9, European Geosciences Union.
- Wessel, P., J. F. Luis, L. Uieda, R. Scharroo, F. Wobbe, W. H. F. Smith, and D. Tian (2019). The Generic Mapping Tools version 6, *Geochem. Geophys. Geosys.* **20**, no. 11, 5556–5564, doi: [10.1029/2019GC008515](https://doi.org/10.1029/2019GC008515).

Manuscript received 12 July 2022
Published online 22 November 2022